Mo Fischer carbene complexes: A DFT study on the prediction of redox potentials

Adebayo A. Adeniyi[a,b], Marilé Landman[c], Jeanet Conradie[a]

[a] Department of Chemistry, University of the Free State, PO Box 339, Bloemfontein, 9300, South Africa
[b] Department of Industrial Chemistry, Federal University Oye Ekiti, Nigeria
[c] Department of Chemistry, University of Pretoria, 02 Lynnwood Road, Hatfield, Pretoria, 0002, South Africa.
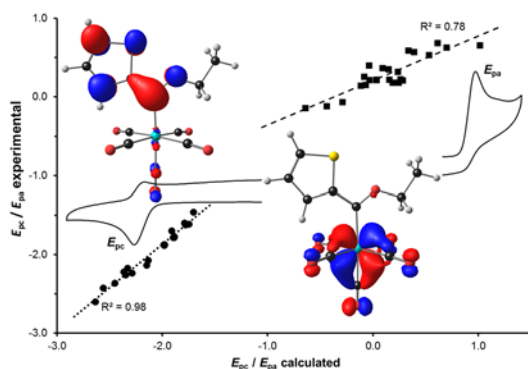
Highlights

Molecular understanding of Mo Fischer carbene oxidation and reduction

Theoretical calculation and prediction of Mo Fischer carbene redox potentials

Electronic effect of ligands and substituents on the redox potential of Mo Fischer carbenes

TOC

TOC entry

The molecular and electronic investigation, understanding and prediction of the oxidation and reduction potential of Mo Fischer carbenes containing different ligands and substituents.

1

Keywords

Abstract

The electronic properties of Fischer carbenes $[Mo(CO)_{5-n}(L_n)\{C(Y)Ar\}]$ (n = 1-2, Ar = aryl group) can be tuned by changing the metal environment and their carbene substituents. The effect of substituting the carbonyl ligands of the carbenes, in the presence of Y = OEt, NH_2 or NHCy as heteroatom substituent, on the redox potential and electronic properties of a series of experimentally known Mo carbenes has been examined using density functional theory methods, to get theoretical ways of predicting the experimental $1e^-$ reduction (M^-) and the $2e^-$ oxidation potential. Several experimental redox potentials - theoretically calculated descriptor relationships were obtained that can be used to predict the reduction and the oxidation potential of the Mo Fischer carbene complexes.

1 Introduction

Since the report of the first Fischer carbene complex, $[W(CO)_5\{C(OEt)Ph\}]$, in 1964 [1], the field of carbene chemistry has grown exponentially. Although the range of transition metals incorporated in Fischer carbene complexes have been expanded [2–4], traditional Fischer carbene complexes contained Group VI transition metals [5–7]. Of these three metals, Mo constitutes the least abundant class of Fischer carbene complexes [8]. Fischer and Maasböl reported the synthesis of the first molybdenum Fischer carbene in 1967 [9].

Substitution of one or more carbonyl ligands on the carbene complex by ligands such as phosphines conveyed additional air stability to the complexes [10–12]. Several arene- and heteroarene Mo Fischer carbene complexes have been structurally characterized, containing phenyl [12–14], thiophene derivatives [15–17], furan [16,18–20], N-methyl pyrrole [15] or ferrocenyl [21,22] as carbene substituents. From the structural data, it is clear that variations in the metal environment and carbene substituent affect the electronic properties of the complexes. This was confirmed in electrochemical studies of Mo carbene complexes, where oxidation occurs at the metal centre and reduction at the carbene carbon atom [23]. A higher, less negative carbene carbon reduction potential and higher, more positive Mo oxidation potential are observed in the series 2-thienyl > 2-furyl > 2-(N-methyl)pyrrolyl as carbene substituents [24]. Substitution of carbonyl ligands reduced the

2

oxidation potential of the complex; the *mer*-[(CO)$_3$(dppe)Mo] carbene complex was easier to oxidize (approximately 0.6 V lower) than the pentacarbonyl Mo carbene analogue [25]. Also, ethoxy carbene complexes are more difficult to oxidize (more than 0.05 V higher) than aminocarbene complexes [25].

In this study, 23 derivatives of Mo carbene complexes are examined (Figure 1). The 23 derivatives are grouped into 5 models which are derivatives of 2-thienyl (model 1), 2-(N-methyl)pyrrolyl) (model 2), 2-(2-thienyl)thiophene (model 3), 2-furyl derivatives (model 4) and 2-furyl with a bidentate diphenyl phosphinoethane (dppe) ligand (model 5). The focus of the study is to find theoretical ways to predict oxidation and reduction potentials (OP and RP) of the Mo Fischer carbene complexes of the type [Mo(CO)$_n$(L$_{n-5}$){C(Y)Ar}] (n = 3-5, Ar = aryl group) and Y = OEt, NH$_2$ or NHCy, to enable the use of these results in predicting the RP and OP of related Mo Fischer carbene complexes.
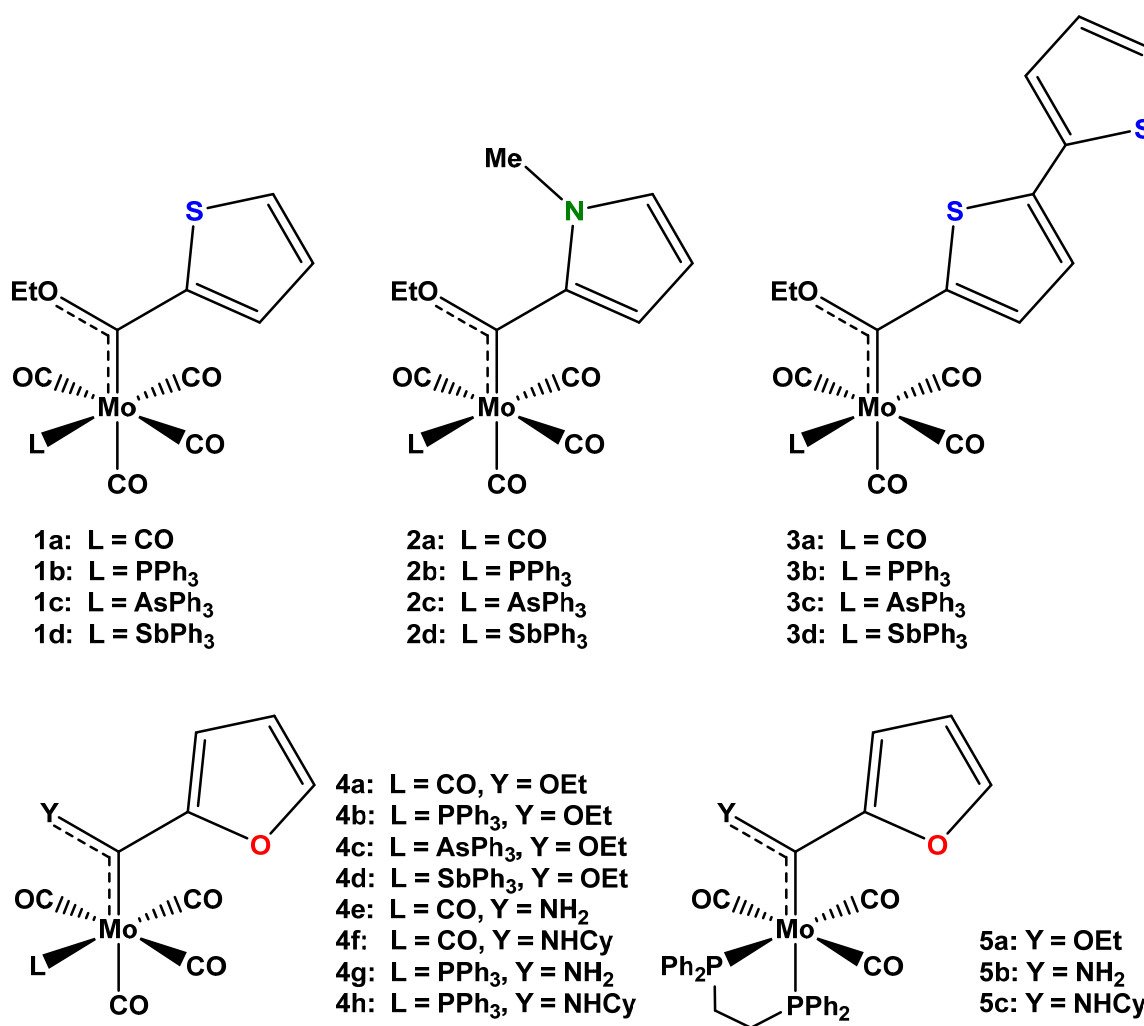

Figure 1: The schematic representation of 23 Mo carbene complexes that are grouped into five models. Only the main isomer of each carbene, for which experimental redox data obtained under the same experimental conditions were available, was used in this study.

2   Computational Methods

All the simulations were carried out using density functional theory (DFT) and the Gaussian 16 program package [26]. The structures of all of the 23 Mo carbene complexes (Figure 1) that were considered in this study were optimized in their neutral (M), reduced (M^-) and oxidized (M^+ and M^{2+}) states (M = molecule) at the gas-phase level of theory using B3LYP and the double zeta-valence polarized basis set 6-31+G(d,p) for all the atoms (C, H, N, O, S, As, P) excluding Mo and Sb atoms that were described with the Def2TZVPP basis set [27] and its pseudopotential to describe the electronic core. The input coordinates for the compounds were constructed using the program Chemcraft [28].

Three types of oxidation potential (OP) and ionization potential (IP) were computed, considering the possibility of 1e⁻ oxidation (M^+), two consecutive 1e⁻ oxidation (M^{++}) and 2e⁻ oxidation (M^{2+}). These three sets of oxidation potential and one reduction potential results in four redox potential calculations for each of the 23 complexes. The calculated solvation energy that was used in the redox potential calculations were carried out in acetonitrile, the experimental solvent, as an implicit solvent and the redox potential was calculated using the energy cycle of solvation shown in Figure 2.

The details of computing the redox potential from the thermodynamic cycle are described in our previous studies [29–31]. The equations that were used can be summarised as follows [32]:

$$E(\text{absolute redox potential}) = \frac{-\Delta G_{rxn}}{nF}$$

$$E_{cell}(vs \text{ reference electrode in V}) = \frac{-\Delta G_{rxn}}{nF} - E_{ref} = \frac{-(\Delta G_{gas}^0 + \Delta\Delta G_{sol})}{nF} - E_{ref}$$

E_{ref} is the absolute redox potential of the reference electrode. The ferrocene (Fc/Fc⁺) redox couple is taken as reference (E_{ref}) in the equation, E_{ref} = Fc/Fc⁺ (= 4.988 V in acetonitrile) [33] and the solvation energies of the redox calculation ($\Delta\Delta G_{sol}$) were determined by:

$$\Delta\Delta G_{sol} = \Delta G_s(M^-) + \Delta G_s(e^-) - \Delta G_s(M) = \Delta G_s(M^-) - \Delta G_s(M) \text{ , since } \Delta G_s(e^-) = 0$$

The expression ΔG_{gas} is the Gibbs free energy of the reaction in the gas phase and it is expressed as:

$$\Delta G°_{gas} = G(M^-) - G(M) = -EA(M) + [\Delta G_{therm}(M^-) - \Delta G_{therm}(M)]$$

where ΔG_{therm} is the thermal correction to the Gibbs free energy of the reaction in the gas phase and EA is the electron affinity in the case of the reduction potential.

The EA and IP values that were used in the above calculation of reduction potential (E_{cell}) and oxidation potential were computed using the all-electron basis set 6-31+G(2df,2p) for all atoms besides Mo and Sb atoms that were described with the Def2TZVPP basis set and its pseudopotential. The interest is to test the efficiency of the functional M06 *versus* B3LYP in computing the redox potential for Mo carbene complexes because M06 is known to be efficient for thermodynamic calculations [34]. The solvation model based on density (SMD) [35]. Default parameters was used for the polarizable continuum model (PCM) of the solvents. This solvation model applies the integral equation formalism variant (IEF-PCM) [36].

The highest occupied molecular orbital (HOMO)-lowest unoccupied molecular orbital (LUMO) overlap and their centroid distance were also analysed in the package Multiwfn [37–40]. The centroid distance between the HOMO and LUMO is calculated from the x, y, z coordinates of the orbitals' centroid:

$$X_i = \int |\emptyset_i(r)|^2 \, xdr; \quad Y_i = \int |\emptyset_i(r)|^2 \, ydr; \quad Z_i = \int |\emptyset_i(r)|^2 \, zdr$$

The centroid distance then computed between orbitals i and j is:

$$D_{ij} = \sqrt{\left(X_i - X_j\right)^2 + \left(Y_i - Y_j\right)^2 + \left(Z_i - Z_j\right)^2}$$

The molecular electrostatic potential (MESP) calculation was carried out using the Multiwfn [41,42] wavefunction analyzer to analyse the wavefunction file obtained from the electrostatic potential calculation in Gaussian 16 program. The calculated MESP parameters include the MESP for the atom (V_{atom}); the minimum (V_{min}) potential values that correspond to the (3, +3) critical points (CP) on the topological analysis of the MESP iso-surface; the maximum (V_{max}) potential that corresponds to a (3, -3) CP; and the saddle points are designated by (3, +1) and (3, -1) CPs [43]. The MESP parameters are calculated from the standard equation for the potential V(r), at a point r expressed as:

$$V(r) = \sum_{A}^{N} \frac{Z_A}{|r - R_A|} - \frac{\rho(r')d^3r'}{|r - r'|}$$

The $\rho(r')$ in the expression is the electron density, N is the total number of nuclei and Z_A in the charge on nucleus A at position R_A. The only possible existence of V_{max} minima are those associated with the nuclei and does not exist in the three dimensions of the MESP surface [37–40]. The calculated V_{max} in this study is simply the most positive or highest value observed in the MESP surface [44–46]. The rendering of the MESP surface was done using visual molecular dynamics (VMD) [47].
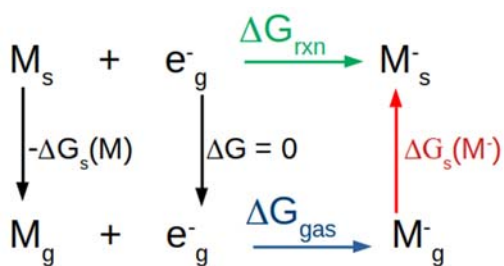
5

Figure 2: The free energy cycle of solvation used in this study for the computation of the redox potential of Fischer Mo carbene complexes M in acetonitrile as solvent. The reduction cycle is shown; the oxidation cycle is similar.

3 Results and discussion

The 1e$^-$ reduction process (M$^-$) of the Mo carbene complexes is known to be mainly located on the carbene C of the carbene ligand, while the oxidation is proposed to be a 2e$^-$ (M^{2+}) transfer process and located on the Mo metal atom [23,25]. The oxidation can also be two discrete or closely overlapping 1e$^-$ oxidation steps (M^{++}) [25,48]. The experimental redox potential values of all of the derivatives (Figure 1), obtained under the same experimental conditions, are available in literature [25] (**4f-h** and 5**a-c**), [49] (**1a-c**, **2a-c**, **3a-c** and **4a-c**) and [24] (**1d**, **2d**, **3d**, **4d**). Although the main goal of this work was to find theoretical ways to predict oxidation and reduction potentials (OP and RP), we first present geometrical and electronic features of the density functional theory optimized geometries of the neutral (M), reduced (M$^-$), 1e$^-$ (M$^+$) and 2e$^-$ (M^{2+}) oxidized molecules, that might influence the OP and RP.

3.1 DFT calculated properties

3.1.1 Geometry and frontier MOs

The DFT optimized geometries of the neutral carbenes, M, in agreement with available structural data [20,50], show that the complexes have a near octahedral arrangement of ligands surrounding the metals. The geometries of the M$^+$ and M$^-$ states are very similar to the geometry of the neutral state M, but the geometry of the doubly oxidized M^{2+} state is severely distorted from octahedral geometry; see supporting information Figures S1 and S2 for the optimized geometries of selected molecules. An analysis of the calculated bond distance between Mo and the carbene carbon atom (Mo-C$_{carbene}$ bond, Figure S3) shows a general trend of the neutral to the reduced and oxidized states in the order of M^{2+} < M^0 < M$^-$ (Figure S3 a), while the Mo-C$_{carbene}$ bond of the neutral (M^0) and 1e$^-$ oxidized (M$^+$)

6

states are the same within 0.04 Å. After reduction, the octahedral metal complex will become a d^7 low spin complex, with an electron in a higher energy orbital, increasing the Mo-C bond length by 0.02 – 0.13 Å. After 2 e$^-$ oxidation, the complex is more electron-deficient, leading to a *ca.* 0.2 Å shortening of the bond to a value of *ca.* 2.05 Å for the Mo-C bond length. However, it is observed that most of the furyl-containing M^{2+} states (**4a** – **4d**, **4g**, **4h** and **5a**), displayed much longer Mo-C bond lengths (> 2.15 Å). Evaluation of the optimized structures of these furyl-containing M^{2+} states (Figure S2) shows that severe distortion from the octahedral orientation of the ligands around the Mo metal occurs. In the other furyl-containing M^{2+} states of **4e**, **4f**, **5b** and **5c**, the furyl ring is rotated 90° with respect to the carbene plane in the neutral ligand, with Mo-C bond lengths of *ca.* 2.05 Å, similar to what was found for the non-furyl containing M^{2+} states.

Neutral Mo and other groups 6 Fischer carbenes are d^6 complexes and the top three occupied orbitals are mainly d$_{xz}$, d$_{yz}$ and d$_{xy}$ character. The d_{z^2} and the $d_{x^2-y^2}$ orbitals are unoccupied and of much higher energy. The LUMO is mainly located on the carbene C, but also distributed over the heteroarene group [51]. An example of the features of the HOMO and LUMO of the neutral, reduced and M$^+$ and M^{2+} oxidized states are shown in Figure 3 for complex **1a** (Mo(CO)$_5$-carbene). Both the HOMO (α) and LUMO (β) of the paramagnetic M$^+$ oxidized state are similar and both of mainly d$_\pi$ character. This is expected, since upon oxidation, β electron is removed from the d$_\pi$ HOMO of the neutral state. The closed-shell HOMO and LUMO of the M^{2+} oxidized state are of mainly d$_\pi$ character. The LUMO of M^{2+} originates from the d$_\pi$ HOMO of the neutral state and the HOMO of M^{2+} originates from the d$_\pi$ HOMO-1 of the neutral state (if no rearrangement of MOs occurs upon oxidation). Both the HOMO (α) and LUMO (β) of the paramagnetic M$^-$ reduced state are similar and both located on the carbene ligand. One electron reduction of a d^6 Mo carbene thus leads to a paramagnetic ($d^6L^\bullet$) state. The character of the HOMO and LUMOs give insight into the locus of the reduction and oxidation of the Mo-carbenes of this study. The 1e$^-$ reduction of the Mo carbenes of this study will mainly occur on the carbene C, while both 1e$^-$ and 2e$^-$ oxidation will be Mo metal-based.

Although the HOMO and LUMO of the Mo carbenes have different energies (see discussion in the next section), they occupy the same space in the molecule. A visualization of the overlap between the HOMO and LUMO of derivative **1a** is shown in Figure 4. Using the centroid of the HOMO and LUMO, the distance between the HOMO and LUMO is determined using Multiwfn, as described in the methodology. The plots of the calculated distance and overlap between HOMOs and LUMOs of the complexes in their neutral, M$^-$ reduced or M$^+$ and M^{2+} oxidation states are shown in Figure S3.

The feature of the centroid distance and overlap between the HOMO and LUMO for carbene derivative **1a** in the neutral and reduced states are shown in Figure 4. The HOMO and LUMO of the neutral state M of derivative **1a** are well separated from each other and consequently lead to a longer distance and less overlap compared to the reduced state M$^-$, where a significant level of overlap was observed (Figure S3) because both the HOMO and LUMO of M$^-$ are of the same character and located on the same carbene ligand (Figure 4). Though the HOMO and LUMO of the neutral complexes are mainly located on Mo and the carbene ligand respectively (Figure 3, Figure 4), there is no direct relation between the HOMO-LUMO distance of the neutral complexes and their Mo-C$_{carbene}$ bond length. The M$^-$ reduced states with longer Mo-C$_{carbene}$ bonds are associated with smaller HOMO-LUMO centroid distances and consequently greater overlapping of the HOMO and LUMO compared to their neutral and M^{2+} oxidation states.

The centroid distance between the HOMO and LUMO is clearly shown as the reverse of the overlap between them, in the complexes where the distance is long, the overlap of the orbitals is less. Among all the derivatives, the unsubstituted CO derivatives (**1a**, **2a**, **4a**, **4e**, **4f**) have longer distances between the HOMO and LUMO and consequently less overlap of the orbitals of their neutral state (except **3a**). The molecules of model 5 have a similar lower overlap than those of the unsubstituted CO derivatives. The highest HOMO-LUMO overlap is observed for both M$^-$ reduced and M$^+$ oxidized states (of which the HOMOs and LUMOs are similar) compared to the neutral and M^{2+} states (with HOMOs and LUMOs of a different character) as well as shorter HOMO-LUMO centroid distances.
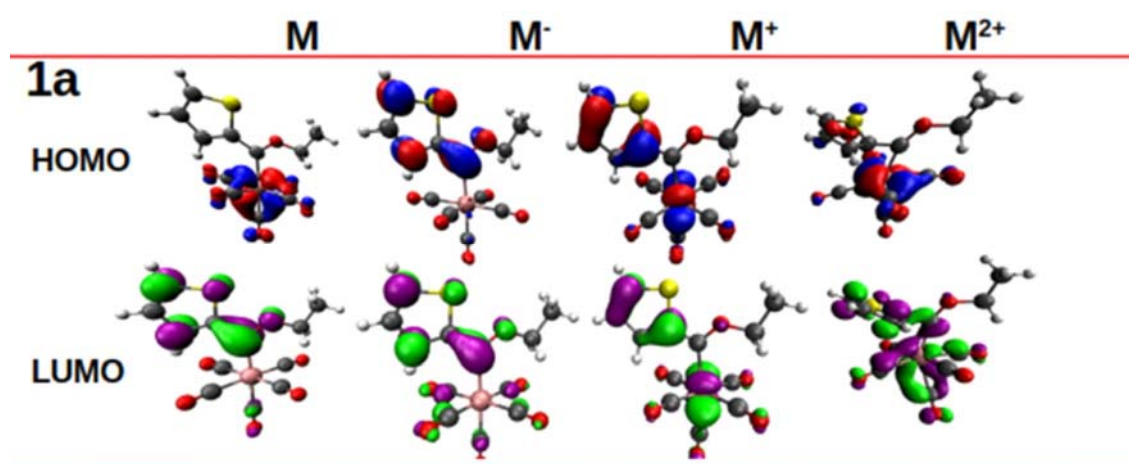

Figure 3: The feature of the HOMO (red/blue isosurface) and LUMO (purple/green isosurface) of complex **1a** in the neutral (M), reduced (M$^-$), and oxidized (M$^+$ and M^{2+}) states. Contour used for MO plots = 0.05 eÅ^{-3}.
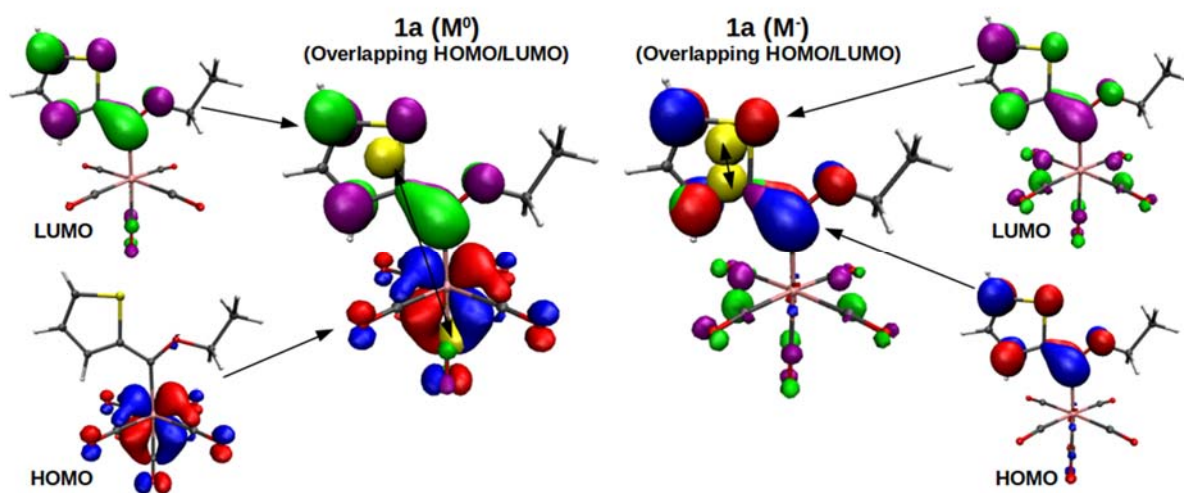
Figure 4: The overlapping of the HOMO (red/blue isosurface) and LUMO (purple/green isosurface) of derivative **1a** in its neutral state (M^0) and reduced state (M^-). The distance between HOMO and LUMO was obtained from the distance between their located centroids (yellow ball) as shown in the image. Contour used for MO plots = 0.05 eÅ^{-3}.

3.1.2   Energies and polarity

The features of the electronic energy, HOMO energy, LUMO energy and the dipole across the five models of the 23 derivatives are shown in Figure S4. The change in their electronic energy, HOMO and LUMO energies from the neutral to the reduced state and also to the oxidized states (1e$^-$ and 2e$^-$ oxidations) are shown in Figure 5. The calculated HOMO-LUMO gap energy of the neutral state relates to the experimental electrochemical HOMO-LUMO gap energy (difference between the first oxidation and first reduction potential), an indication of the reliability of the calculated frontier orbital energies, see Figure 6. This relationship can also be used to predict the oxidation potential or reduction potential if one of them fall out of the experimental solvent window.

3.1.2.1   *Effect of reduction*

In comparison to the neutral state of the derivatives, reduction lowers the electronic energy (with the electron affinity value) but raises the HOMO (with *ca*. 0.09 au) and the LUMO (with *ca*. 0.03 au) energies of the complexes. The energy of the SOMO (singly occupied molecular orbital) of the reduced state, where the electron was added upon reduction, thus rises relative to the energy of the HOMO of the neutral state, but it is still lower relative to the higher energy LUMO of the neutral state from where it originates from. The energy of the SUMO (singly unoccupied molecular orbital) of the reduced state is higher than the energy of the LUMO of the neutral state from where it originates from. The HOMO of the neutral state now becomes the HOMO-1 of the reduced state (if no rearrangement of MOs occurs upon reduction). In addition, the HOMO-LUMO gap energy decreases

9

in going from the neutral to the reduced state, implying the reduced state is more reactive and less stable than the neutral state.

3.1.2.2 Effect of oxidation

However, in comparison to the neutral state of the derivatives, oxidation raises the electronic energy (with the ionization potential value) but lowers both the HOMO (with *ca*. 0.05 au) and LUMO (with *ca*. 0.07 au) energies. There are unique differences in the M^+ and M^{2+} oxidations; the HOMO energy is ca 0.03 au lower for the closed-shell diamagnetic 2e⁻ oxidation (M^{2+}) than for the 1e⁻ paramagnetic oxidation (M^+) state, implying that removal of the second electron (from the neutral carbene), stabilizes the HOMO. The HOMO of the M^+ state is of the same character as the HOMO of the neutral state, but only with an α electron in it (the β electron was removed upon oxidation), while the HOMO of the M^{2+} state is of the same character than that of the lower energy HOMO-1 of the neutral state. The LUMO energy of the 2e⁻ oxidation is higher than that of the 1e⁻ oxidation (except for **3b**), implying that the HOMO-LUMO gap energy increases for M^{2+} (lower HOMO and higher LUMO) compared to M^+, making M^{2+} more stable compared to the paramagnetic intermediate M^+ state.

3.1.2.3 Dipole

The general feature of the dipole (Figure S4) shows that the polarity of the molecules increases in reduced complexes, leading to higher dipole moments than in the neutral and oxidized states. Exceptions are complexes **1a**, **2a**, **3a**, **4a**, **4e** and **4f**, all of C_s symmetry, where none of the five CO ligands has been substituted. The higher polarity of the reduced molecules is due to the unpaired electron density added upon reduction, which is located on the carbene C and also distributed over the carbene ligand, leading to a difference in electronegativity between the carbene ligand and the $Mo(CO)_nL_m$ unit (n = 3 or 4, m = 5 − n). The lower polarity of the oxidized complexes is more pronounced in the M^+ oxidized complexes compared to the M^{2+} oxidized complexes (Figure S4). Since oxidation occurs on the metal, the change in electron density on the central metal does not lead to such a large change in polarity between the different ligands in the molecule, compared to reduction.
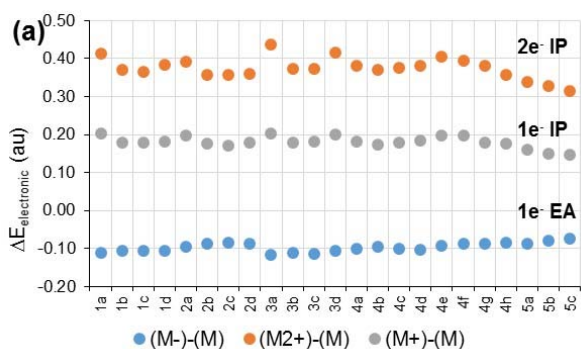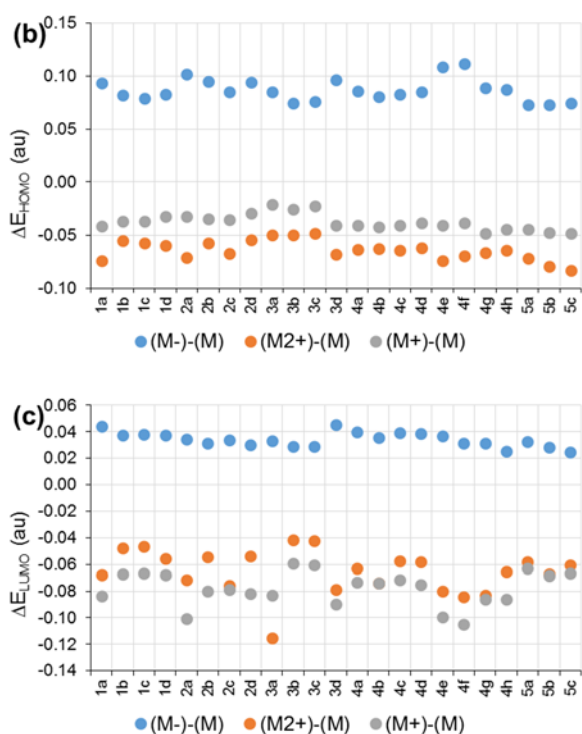
Figure 5: The change in (a) the electronic energy ($M^{-/+/2+} - M^0$), (b) HOMO and (c) LUMO energies of the complexes from the neutral state (M^0) to the indicated redox state ($M^{-/+/2+}$), calculated in acetonitrile using the B3LYP/ 6-31+G(d,p)/def2tzvpp gas-phase optimized geometry. All energies have been reported in au (1 au = 27.2114 eV).
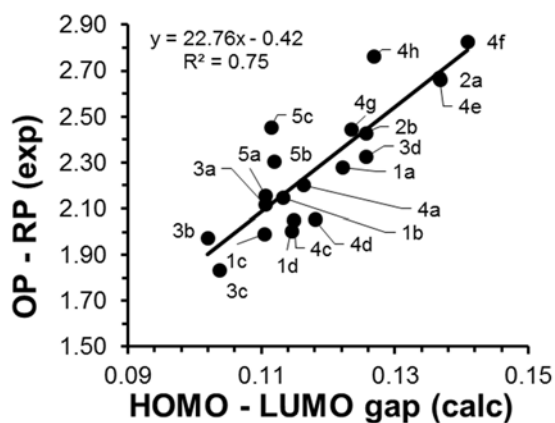

Figure 6: Relationship between the experimental electrochemical HOMO – LUMO gap (OP – RP in V) and the B3LYP/ 6-31+G(d,p)/def2tzvpp gas-phase calculated HOMO – LUMO gap in au (1 au = 27.2114 eV) for the complexes of this study.

3.1.2.4 Effect of CO substitution

In neutral complexes, higher HOMO energy is associated with a lower IP value (less energy needed to remove the electron from the HOMO) while a higher LUMO energy is associated with a smaller absolute EA value (more difficult to add the electron to a higher energy LUMO). From Figure 5 we observe that reduction of the complexes has a stronger effect on the HOMO energy while oxidation has a stronger effect on the energy of the LUMO; reduction increases the energy of the HOMO with *ca*. 0.09 au, while reduction increases the energy of the LUMO with *ca*. 0.03 au. The calculated electron affinity (EA) and calculated ionization potential (IP) values are shown in Figure 5 (a) as the change in the energy from the neutral state to their reduced (M^- - M^0) and oxidized ($M^{+/2+}$ - M^0) states respectively. The complexes where the five CO ligands have not been substituted as found in the first four models, *i.e.* the unsubstituted $[Mo(CO)_5\{C(Y)X\}]$ complexes (**1a**, **2a**, **3a**, **4a**, **4e** and **4f**) have higher ionization potential (IP) values for their M^+ and M^{2+} oxidation processes compared to the rest of the derivatives in each of the first four models (Figure 5), implying these complexes are more stable against oxidation (related to IP). It was indeed experimentally found that the unsubstituted $[Mo(CO)_5\{C(Y)X\}]$ complexes (**1a**, **2a**, **3a**, **4a**, **4e** and **4f**) have a higher experimental oxidation potential than the rest of the investigated complexes, as predicted by the higher calculated IP values. The same unsubstituted CO complexes also have higher HOMO energy values of their reduced states, (HOMO of reduced state, i.e. the SOMO, the MO where the electron was added upon reduction) but lower LUMO energy values of their oxidized states (LUMO of the oxidized state is the MO where the electron was removed upon oxidation) compared to the rest of the derivatives in each model (model **1** – model **5**, Figure 1). (SOMO = singly occupied HOMO). For OEt derivatives with unsubstituted CO ligands (**1a**, **2a**, **3a**, **4a**, **4e** and **4f**), the higher HOMO energy in the reduced state and lower LUMO energy in the M^{2+} oxidized state, correspond linearly to higher EA (less negative or smaller absolute value) and higher IP values respectively.

3.1.2.5 Effect of NH₂ and NHCy substitution

Substitution of the Y position (the heteroatom group) of the models with NH_2 and NHCy substituents leads to higher HOMO energies of the reduced species and lower LUMO energies of the oxidized species compared to the OEt complexes. For example, the presence of carbene substituents NH_2 and NHCy on complexes **4e** and **4f** results in higher HOMO energies of the reduced state and lower LUMO energy of the oxidized state compared to **4a** with OEt. The effect of substituents NH_2 and NHCy in increasing HOMO energy of the reduced species and lower LUMO energy of the oxidized species compared to the presence of an OEt substituent is also reflected in the data of derivatives **4g** and **4h** compared to **4b**, and **5b** and **5c** compared to **5a.** This consequently leads to higher EA (less negative or smaller absolute value) but lower IP of the derivatives with NH_2 and NHCy substituents

12

compared to those with an OEt group of the same molecule (models 4 and 5, Figure 1). Experimentally, indeed, a lower reduction potential (associated with a higher less negative EA or smaller absolute EA value) and lower oxidation potential (associated with a lower/smaller IP) were obtained for the derivatives with NH$_2$ and NHCy substituents compared to those with an OEt group [25]. Generally, the type of model also affects the EA in the order of **3** < **1** < **2** < **4** < **5** while the IP follows the reverse order of **5** < **4** < **2** < **1** < **3**.

3.1.3 MESP potentials

Some of the important applications of the MESP analysis include its application as a descriptor of reactivity and stabilities of chemical and biological molecules [52,53], its use to determine the total electronic effect of ligands (eeL) and the MESP potential is also used to predict the reduction potential of molecules [52,54].

The surface and location of the V_{min} and V_{max} with their values are shown in Figure 7 for the complex **1a** and **5c** in the neutral, M$^-$ reduced, M$^+$ and M^{2+} oxidation states. The V_{min} and V_{max} change in values and position as the molecules change from neutral to reduced and oxidized states (Figure 7). The change in the position of V_{min} with redox states is an indication of a change in the reaction site of the complexes around the ligands. For a neutral molecule, V_{min} is near one of the O_{CO} atoms.

The trend in the MESP variables V_{min}, V_{max}, V(Mo) and V(C) of the coordinating carbene carbon across the 23 complexes is shown in Figure 8 with data in Table S2-S3. The M$^-$ reduction resulted in lower values of the MESP variables V_{min}, V_{max} and V_{Mo} while M$^+$ and M^{2+} oxidation lead to higher potential values compared to the neutral state. The M^{2+} oxidation has the highest values of the MESP potential values. Figure 9 highlights the change in the V(Mo) and V(C) values for the complexes of the neutral state. The presence of dppe ligands in model 5 led to much lower values of the MESP variables V_{min}, V(Mo) and V(C) compared to the unsubstituted CO derivatives. The presences of PPh$_3$, AsPh$_3$ or SbPh$_3$ ligands also led to lower MESP properties than the derivatives with unsubstituted CO ligands (**1a**, **2a**, **3a**, **4a**, **4e** and **4f**), similar to dppe ligands.
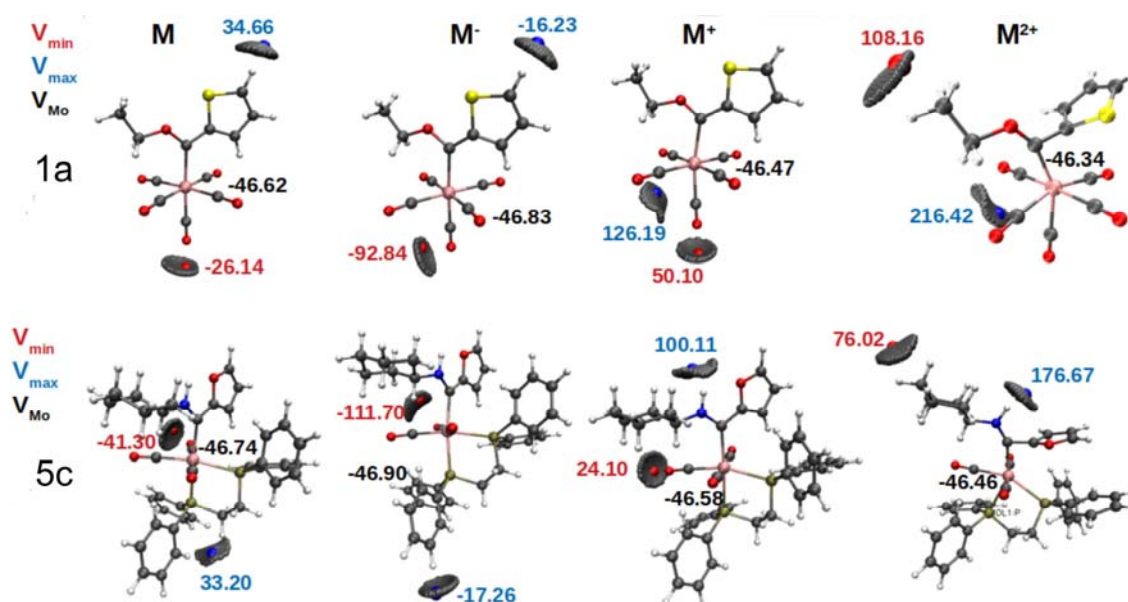
Figure 7: The MESP surface of the complexes **1a** and **5c** in their neutral, M⁻ reduced, M⁺ oxidized, M^{2+} oxidized states showing the MESP minimum (V_{min}), maximum (V_{max}) and that of Mo atom (V(Mo) indicated as V_{Mo}). The V_{min} and V_{max} are reported in kcal/mol while V_{Mo} is in atomic unit.

Figure 8: The change in the MESP potentials (a) V(max), (b) V(min), (c) V(Mo) and (d) V($C_{carbene}$) across the 23 derivatives in the neutral, reduced, M⁺ and M^{2+} oxidised states.

Figure 9: The change in the MESP potential (a) V(Mo) and (b) V($C_{carbene}$) for the 23 derivatives in the neutral state. The L substituent in $Mo(CO)_nL_{5-n}$ is indicated. For n = 5, L = CO, n= 4, L = PPh_3, $AsPh_3$ or $SbPh_3$ and for n = 3, L = dppe.
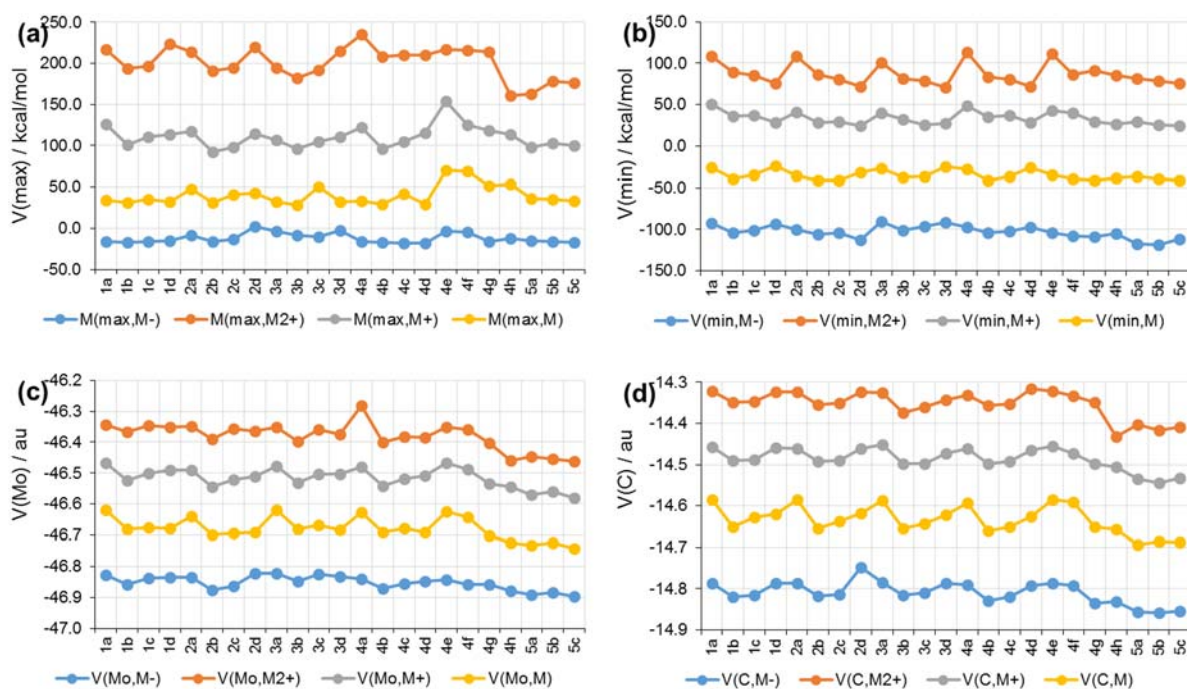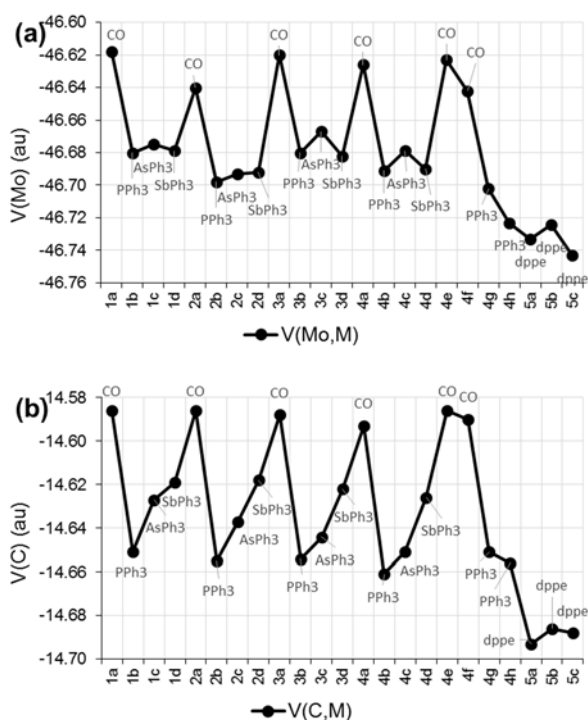
3.2 Theoretical determination of reduction and oxidation potential

3.2.1 Calculation of reduction and oxidation potential

The available experimental reduction and oxidation potential values of the 23 Mo carbene complexes in this study (Figure 1) are shown in Table 1, in addition to the calculated reduction and oxidation ($1e^-$ and $2e^-$) potential values using B3LYP and M06 functional methods; also see Figure 10. Generally, the experimental reduction and oxidation potential values have similar features across the derivatives; the derivatives with high reduction potential are also observed to show a high oxidation potential. Among the three sets of oxidation states M^+, M^{++} and M^{2+}, the M^+ has, as expected, the lowest oxidation potential compared to the M^{++} and M^{2+} states. The experimental and calculated reduction potential values show a similar pattern of changes across derivatives within a close range (Figure 10).

The unsubstituted CO derivatives, especially those with an EtO substituent, have the highest reduction and oxidation potential values (Figure 10). This agrees with the experimental report that ethoxy carbenes are more difficult to oxidize (more than 0.05 V higher) than aminocarbenes [25]. The plots

15

of the experimental reduction potential and that of the calculated reduction potential using M06 (R^2 = 0.97) and B3LYP (R^2 = 0.98) (Figure 10) shows that B3LYP behave slightly better than M06, also because of lower mean absolute deviation (MAD 0.124 vs 0.151), as shown in Table 1. Across all the derivatives, the B3LYP calculated reduction potential show lower MAD (0.124) compared to the oxidation states M^+ (0.395), M^{++} (0.214) and M^{2+} (0.196). A higher value of MAD of M^+ oxidized derivatives from that of the experimental is an indication that the experimentally observed oxidation are not M^+ (1 e⁻) oxidation but M^{++} or M^{2+} (both 2 e⁻) oxidation.

The experimentally measured two-electron oxidation potential is related to the B3LYP calculated two-electron oxidation potential using the M^{++} and M^{2+} models (see Figure 12 and the supplementary information Figure S5 for relationships involving the M06 calculation). A higher correlation between the experimentally measured two-electron oxidation potential and the calculated two-electron oxidation potential using the M^{2+} model is obtained, with R^2 = 0.78 (B3LYP) and 0.77 (M06), indicating that many of the experimental oxidation processes probably occur through 2e⁻ a process rather than M^{++}. Though M^+ calculated OP values highly deviate from the experimental compared to those obtained from M^{++} and M^{2+}, M^+ gave better experimental correlation with R^2=0.90 (B3LYP) and R^2=0.91 (M06), clearly showing that the experimental oxidation potential strongly depends on the ease of removing the first electron through a paramagnetic M^+ state.

The higher correlation of the computed reduction and oxidation potential from B3LYP with the experimental reduction and oxidation potential compared to those calculated with the M06 functional (Figure 11, Figure 12, Figure S5), shows that B3LYP performs better than M06, in addition to the lower MAD of B3LYP (Table 1), in calculating the reduction potential of Mo Fischer carbenes of the type $[Mo(CO)_n(L_{n-5})\{C(Y)Ar\}]$ (n = 3-5, Ar = aryl group) and Y = OEt, NH_2 or NHCy.
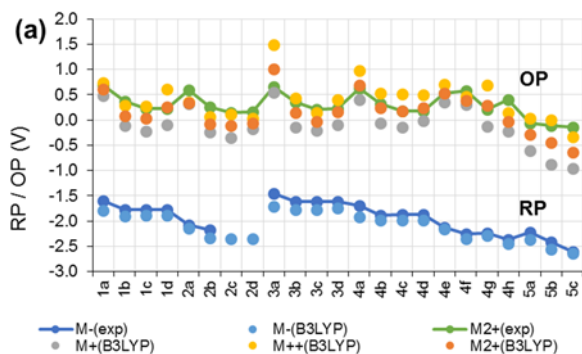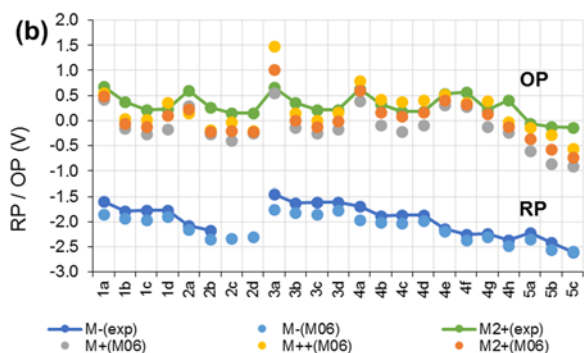
Figure 10: The experimental and calculated reduction and oxidation potentials of the derivatives using (a) B3LYP and (b) M06 functional methods. The calculated oxidation potential for the M^+, M^{++} and M^{2+} types of calculated oxidation potentials of the derivatives are shown. Experimental values are emphasized with a solid line.

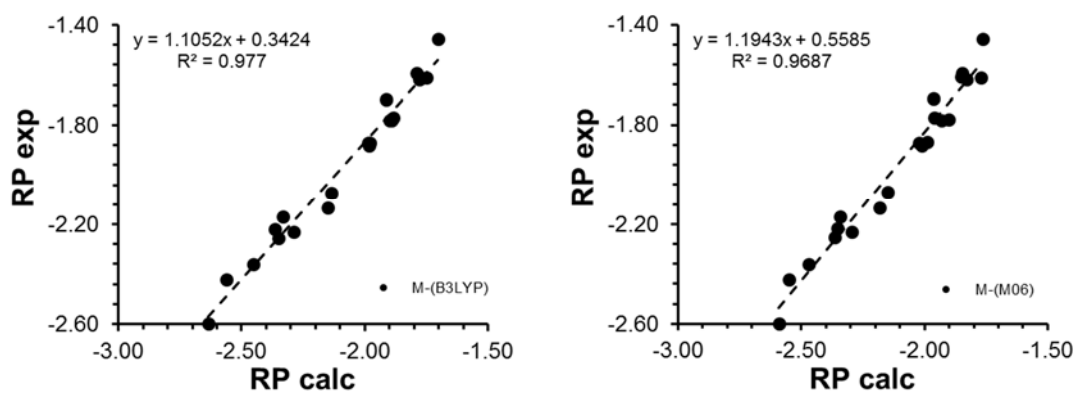Figure 11: The correlation of the experimental and computed reduction potential (RP) values (in V *versus* Fc/Fc$^+$) of the 23 derivatives using B3LYP and M06 functional methods. The unit is in V.
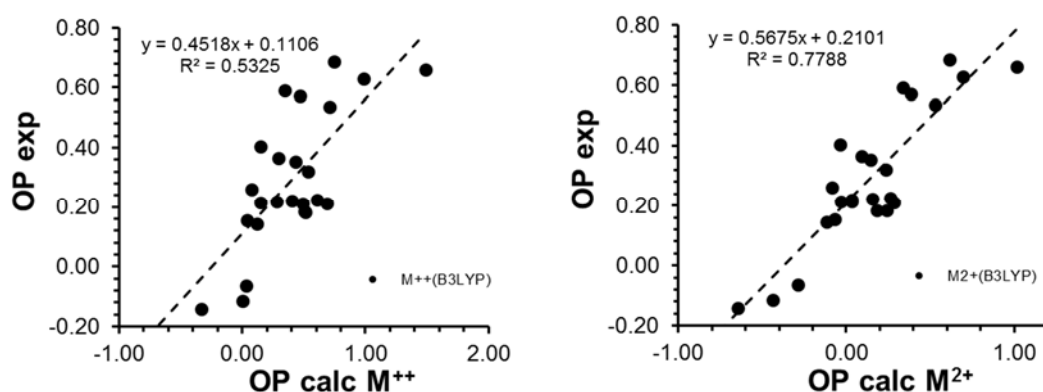

Figure 12: The correlation of the experimental and B3LYP computed (M^{++} and M^{2+}) oxidation potential values (in V *versus* Fc/Fc$^+$) of the 23 derivatives using the B3LYP functional method.

Table 1: The experimental double electron oxidation (M^{2+}) and single-electron reduction (M^-) potential of the Mo-carbene complexes and their computed single reduction, single oxidation (M^+), double sequential single-electron oxidation (M^{++}) and double electron oxidation (M^{2+}) potential values using M06 and B3LYP functional method.

	M^{2+}(exp)	M^-(exp)	M^-(M06)	M^-(B3LYP)	M^+(M06)	M^+(B3LYP)	M^{++}(M06)	M^{++}(B3LYP)	M^{2+}(M06)	M^{2+}(B3LYP)
1a	0.686	-1.594	-1.848	-1.790	0.430	0.479	0.552	0.745	0.491	0.612
1b	0.367	-1.781	-1.930	-1.898	-0.151	-0.116	0.034	0.293	-0.059	0.089
1c	0.219	-1.771	-1.961	-1.886	-0.259	-0.218	0.021	0.280	-0.119	0.031
1d	0.226	-1.779	-1.902	-1.890	-0.164	-0.087	0.366	0.609	0.101	0.261
2a	0.592	-2.071	-2.149	-2.134	0.299	0.324	0.153	0.348	0.226	0.336
2b	0.261	-2.170	-2.344	-2.332	-0.259	-0.242	-0.184	0.073	-0.222	-0.085
2c	0.144	-	-2.337	-2.346	-0.387	-0.358	-0.031	0.121	-0.209	-0.118
2d	0.154	-	-2.296	-2.357	-0.243	-0.177	-0.200	0.037	-0.222	-0.070
3a	0.660	-1.458	-1.764	-1.704	0.557	0.541	1.478	1.485	1.017	1.013
3b	0.353	-1.620	-1.828	-1.780	-0.144	-0.138	0.143	0.430	-0.001	0.146
3c	0.215	-1.609	-1.850	-1.778	-0.254	-0.212	0.007	0.145	-0.123	-0.033
3d	0.222	-1.611	-1.771	-1.749	-0.166	-0.090	0.162	0.400	-0.002	0.155
4a	0.630	-1.696	-1.964	-1.912	0.387	0.407	0.797	0.984	0.592	0.696

4b	0.322	-1.882	-2.012	-1.984	-0.089	-0.060	0.419	0.534	0.165	0.237
4c	0.183	-1.870	-2.023	-1.980	-0.216	-0.144	0.375	0.512	0.080	0.184
4d	0.185	-1.869	-1.988	-1.987	-0.082	-0.020	0.402	0.504	0.160	0.242
4e	0.537	-2.133	-2.184	-2.150	0.316	0.352	0.512	0.709	0.414	0.530
4f	0.572	-2.255	-2.366	-2.349	0.276	0.306	0.362	0.468	0.319	0.387
4g	0.212	-2.232	-2.296	-2.287	-0.120	-0.123	0.395	0.688	0.138	0.283
4h	0.404	-2.360	-2.472	-2.452	-0.231	-0.223	-0.024	0.147	-0.128	-0.038
5a	-0.063	-2.219	-2.355	-2.365	-0.598	-0.612	-0.142	0.035	-0.370	-0.289
5b	-0.115	-2.421	-2.552	-2.562	-0.861	-0.881	-0.276	0.002	-0.568	-0.439
5c	-0.142	-2.598	-2.591	-2.635	-0.899	-0.953	-0.562	-0.335	-0.731	-0.644
MAD			**0.151**	**0.124**	**0.421**	**0.394**	**0.248**	**0.214**	**0.286**	**0.196**

The experimental values from [25] (**4f** and **4g** and 5**a-c),** are taken from the same literature while those of [49] (**1a-c**, **2a-c**, **3a-c** and **4a-c)** and [24] (**1d**, **2d**, **3d**, **4d**).

Instead of considering the experimental oxidation of all 23 derivatives to relate to the calculated $2e^-$ (M^{2+}) transfer process [23,25] (Figure 12 and S5), it could also be considered that the experimental oxidation can be two discrete or closely overlapping $1e^-$ oxidation steps (M^{++}) [25,48] in some cases. Thus, some carbenes could go through a M^{2+} oxidation while the rest of the carbenes predominantly go through a M^{++} oxidation. The results in Figure 10 also show that in the derivatives where oxidation potential from M^{++} is found close to that of the experimental value, the M^{2+} process shows higher deviation and the reverse is also the case where M^{2+} is close to the experimental value. This is an indication that some of the derivatives undergo direct M^{2+} oxidation while others will preferentially undergo two consecutive $1e^-$ oxidation (M^{++}) through a paramagnetic M^+ state. The calculated oxidation potential of the derivatives is then grouped into two groups; the first are those that will preferentially undergo M^{++} oxidations which are **1a-c**, **2a-d**, **3b**, **3c**, **4f, 4h, 5a-c** and those that preferentially show M^{2+} oxidation which is **1d**, **3d**, **4a-e** and **4g**. Among the 23 complexes, fourteen complexes are shown to be M^{++} oxidation and are predominantly the model 1, 2, 3 and 5 complexes while eight complexes are shown to follow M^{2+} oxidation and are predominantly model 4 complexes and those containing ligand SbPh$_3$, excluding the model 2 SbPh$_3$ complex. Only complex **3a** is shown to have a value OP of the M^+ state closer to the experimental value than the M^{++} and M^{2+}states. However, similar correlation values of computed and experimental oxidation potential were obtained for the two separate groups of the oxidation potential using the selected complexes for M^{++} oxidation potential ($R^2 = 0.77$ using B3LYP) and others for M^{2+} oxidation potential ($R^2 = 0.83$ using B3LYP) (Figure S6) compared to the correlation of the M^{2+} oxidation with all the derivatives ($R^2 = 0.78$ using B3LYP, Figure S5, Figure 12).

3.2.2 Prediction of the reduction and oxidation potential from LUMO and HOMO energies

Plotting the B3LYP calculated HOMO and LUMO energies (Figure S4 a and b, Table 2) against the experimental OP and RP, leads to linear relationships (Figure 13) that can be used to predict OP and RP of Mo Fischer carbene complexes of the type $[Mo(CO)_n(L_{n-5})\{C(Y)Ar\}]$ ($n = 3-5$, Ar = aryl group) and Y = OEt, NH$_2$ or NHCy, and related Mo Fischer carbene complexes. The experimental RP value relates to the LUMO energy of the neutral carbene (the MO where the electron is added upon reduction), as well as to the HOMO energy of M^- (MO where the added electron resides after reduction), Figure 13a. The experimental OP value relates to the HOMO energy of the neutral carbene (the MO where the electron is removed from upon oxidation), the HOMO energy of M^+ (related to the MO with an α electron of which the β electron was removed from upon oxidation) and the LUMO energy of M^+ (related to the MO from which the α electron was removed from upon oxidation), see Figure 13b. Using the following linear relationships involving the LUMO (for RP, Figure 13a) and

20

HOMO (for OP, Figure 13b) energies of the neutral carbenes, the RP and OP of the carbenes can be predicted (see Table 2) to a MAD value of 0.058 (RP) and 0.104 (OP) respectively:

RP $_{exp, predict}$ = -24.406 x E(LUMO) - 3.9502   (R^2 = 0.94)   Equation 1

OP $_{exp, predict}$ = -14.815 x E(HOMO) - 2.671   (R^2 = 0.66)   Equation 2

These MAD values for predicting RP and OP from the LUMO and HOMO energy of the neutral carbenes respectively are both lower than all the MAD values obtained when formally calculating the RP and OP (Table 1). To calculate the LUMO and HOMO energy of the neutral carbenes, involve optimizing only the neutral carbene, while the calculation of the RP and OP also need optimization of the reduced and oxidized carbenes, more than double the amount of calculations additionally. Because of the cost of CPU hours, predicting RP and OP from the LUMO and HOMO energy of the neutral carbenes respectively, is a much shorter, easier and cheaper, but also more accurate method (according to the MAD values).
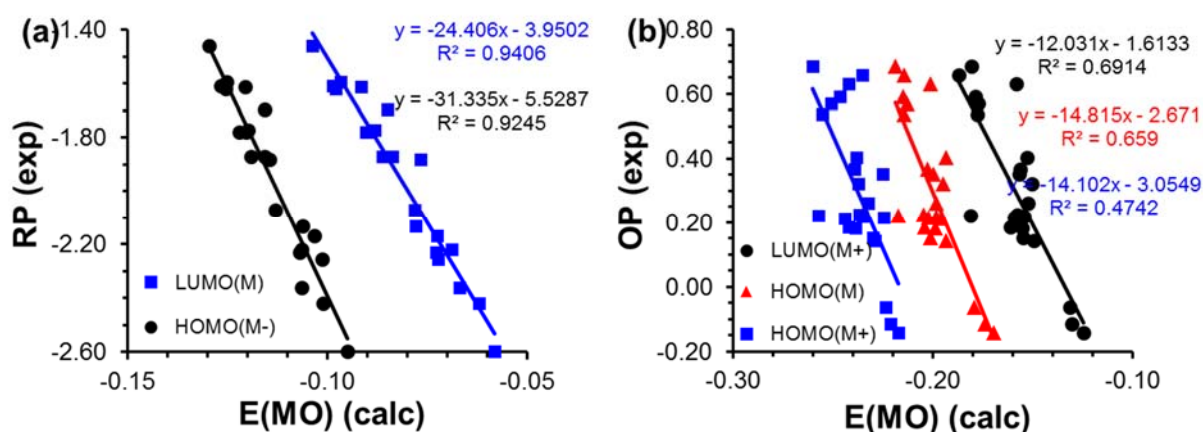
Figure 13: The correlation of the (a) experimental RP with calculated LUMO energy of M and HOMO energy of M$^-$ and (b) experimental OP with calculated HOMO energy of M, HOMO and LUMO energies of M$^+$, using B3LYP in acetonitrile.

Table 2: The experimental RP and OP, B3LYP calculated HOMO and LUMO energies of the neutral carbene, with the predicted RP and OP calculated from the respective frontier orbital energies.

Mol	Experimental RP and OP (V)		Calculated energies (au)		Predicted RP and OP (V)[a]	
	RP(exp)	OP(exp)	LUMO	HOMO	RP from E (LUMO)	OP from E (HOMO)

1a	-1.594	0.686	-0.0968	-0.2189	-1.587	0.573
1b	-1.781	0.367	-0.0894	-0.2026	-1.768	0.331
1c	-1.771	0.219	-0.0882	-0.1986	-1.797	0.271
1d	-1.779	0.226	-0.0904	-0.2049	-1.744	0.364
2a	-2.071	0.592	-0.0781	-0.2149	-2.043	0.513
2b	-2.17	0.261	-0.0727	-0.1982	-2.177	0.266
2c	-	0.144	-0.0711	-0.1937	-2.216	0.199
2d	-	0.154	-0.0734	-0.2012	-2.158	0.310
3a	-1.458	0.66	-0.1039	-0.2145	-1.413	0.506
3b	-1.62	0.353	-0.098	-0.1999	-1.560	0.290
3c	-1.609	0.215	-0.0987	-0.2024	-1.542	0.327
3d	-1.611	0.222	-0.0916	-0.2173	-1.714	0.548
4a	-1.696	0.63	-0.0851	-0.2013	-1.874	0.311
4b	-1.882	0.322	-0.0767	-0.195	-2.078	0.218
4c	-1.87	0.183	-0.0839	-0.1988	-1.902	0.274
4d	-1.869	0.185	-0.0862	-0.2042	-1.847	0.353
4e	-2.133	0.537	-0.0781	-0.2147	-2.044	0.510
4f	-2.255	0.572	-0.0724	-0.2133	-2.183	0.489
4g	-2.232	0.212	-0.0728	-0.1962	-2.174	0.235
4h	-2.36	0.404	-0.067	-0.1938	-2.316	0.200
5a	-2.219	-0.063	-0.0689	-0.1795	-2.270	-0.012
5b	-2.421	-0.115	-0.0621	-0.174	-2.435	-0.094
5c	-2.598	-0.142	-0.0581	-0.1696	-2.531	-0.159
MAD					**0.058**	**0.104**

[a] Equations 1 and 2 used, obtained from graphs in Figure 13.

3.2.3 Prediction of the reduction and oxidation potential from the EA and IP

The EA and IP values in Table 3 were calculated using functional method B3LYP in acetonitrile, while the gas phase EA and IP values were used for the calculation of the RP and OP. The NH_2, NHCy and dppe substituted complexes lead to higher EA and lower IP values (Figure 5a) than the other complexes, which consequently leads to lower reduction potential and oxidation potential (Figure 10) to as previously explained. The calculated EA generally follows the same order that was observed in the reduction and oxidation potential of the complexes.

A good correlation was observed between the experimental 1e$^-$ RP and B3LYP calculated 1e$^-$ EA (R^2 = 0.99, Figure 14a). Good correlations between the experimental 2e$^-$ OP with the three IP values of M$^+$, M^{++} and M^{2+} were also observed. The correlation of the 2e$^-$ experimental OP with 1e$^-$ IP of M$^+$ is R^2 = 0.89 as shown in Figure 14b, while that of the 2e$^-$ IP of M^{2+} is R^2 = 0.81 (Figure 14c) and for M^{++} R^2 = 0.59 (Figure 14d). A better correlation is observed for M^{++} (R^2 = 0.785) and M^{2+} (R^2 = 0.829) if selected derivatives that gave the lowest deviation of their calculated OP from experimental are used (as discussed in the last paragraph of Section 3.2.1, see Figure S7). Oxidation of Mo from Mo(0) to Mo(II) should go through a paramagnetic M$^+$ state in all cases. The linear equations generated for the prediction of experimental 1e$^-$ reduction potential (RP) from B3LYP calculated EA and for the prediction of 2e$^-$ experimental oxidation potential (OP) from B3LYP calculated IP are shown below:

RP $_{exp, predict}$ = -25.96 x EA(M$^-$) - 4.513	(R^2 = 0.99)	Equation 3
OP $_{exp, predict}$ = 14.69 x IP(M$^+$) – 2.361	(R^2 = 0.89)	Equation 4
OP $_{exp, predict}$ = 7.521 x IP(M^{2+}) – 2.519	(R^2 = 0.81)	Equation 5
OP $_{exp, predict}$ = 12.67 x IP(M^{++}) – 2.156	(R^2 = 0.59)	Equation 6

The experimental 1e$^-$ reduction potential and 2e$^-$ oxidation potential were predicted from equations 3 – 6 above and the results of the prediction are shown in Table 3. The prediction reproduced the experimental 1e$^-$ RP from calculated EA and experimental 2e$^-$ OP from calculated IP (of M$^+$, M^{2+} and M^{++}), to a significant level of accuracy with MAD values of 0.023, 0.065, 0.076 and 0.124 respectively, even better than the MAD of 0.058 (RP) and 0.104 (OP) obtained when predicting RP and OP from the HOMO and LUMO energies of the neutral carbene (Table 2).

In terms of reproducing the experimental results, the predicted 2e$^-$ OP from calculated 1e$^-$ IP of M$^+$ (Table 3, MAD = 0.065) is better than from the calculated 2e$^-$ OP (Table 1, B3LYP) for both M^{++} (MAD = 0.124) and M^{2+} (MAD = 0.196). Thus predicting the 2e$^-$ experimental OP from the 1e$^-$ IP of M$^+$, gives more accurate OP values; in some molecules a higher OP is observed while in other cases a lower OP than those predicted from M^{++} and M^{2+}, in a way that more accurately reproduce the experimental OP results.

The predicted RP from EA (Table 3, MAD = 0.023) is also better than the calculated RP (Table 1, B3LYP, MAD = 0.124). This is an indication that the EA and IP values that have been computed in the same solvent medium used for their respective experimental RP and OP processes can predict their RP and OP to a high level of accuracy. Predicting the experimental 2e$^-$ OP using equations 5 and

23

6 above (from EA and IP, MAD values of 0.076 and 0.124 respectively), reproduced the experimental 2e⁻ OP to a lower level of accuracy than using equations 1 and 2 (from HOMO and LUMO energies, MAD values of 0.058 and 0.104 respectively), but was still better than the calculated 1e⁻ RP (MAD = 0.124), the calculated 1e⁻ OP for M⁺ (MAD = 0.394), calculated 2e⁻ OP for M⁺⁺ (MAD = 0.214) and calculated 2e⁻ OP for M²⁺ (MAD = 0.196) (Table 1, B3LYP) using the redox cycle in Figure 2.
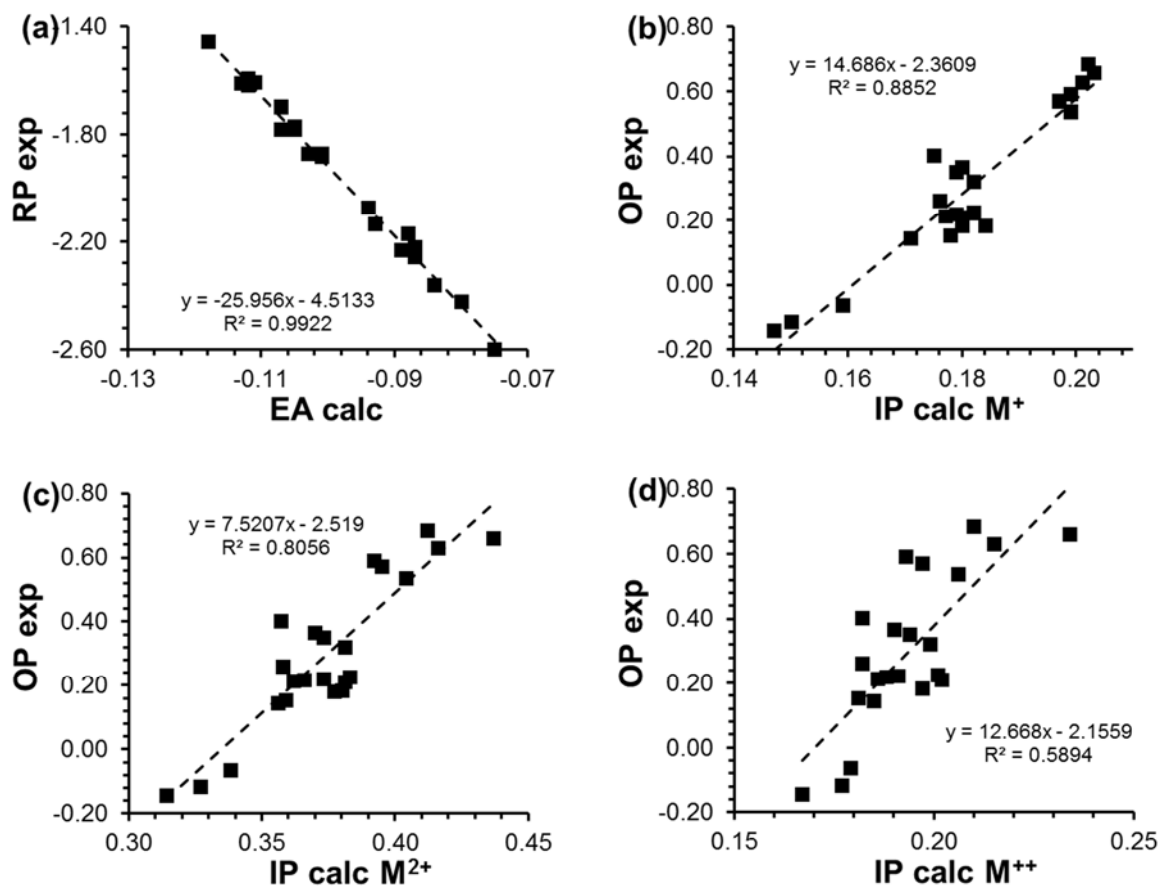

Figure 14: The correlation of the (a) experimental RP with calculated EA of M⁻ and experimental 2e⁻ OP with calculated (b) 1e⁻ IP of M⁺, (c) 2e⁻ IP of M⁺⁺ and (d) 2e⁻ IP of M²⁺ using B3LYP in acetonitrile.

Table 3: The experimental RP and OP, calculated EA and IP (1e⁻ IP for M^+ and 2e⁻ IP for M^{++} and M^{2+}) with the predicted 1e⁻ RP and 2e⁻ OP from the respective B3LYP calculated EA and IP using B3LYP in acetonitrile solution.

Mol	Experimental RP and OP (V)		Calculated EA and IP (eV)				Predicted 1e⁻ RP and 2e⁻ OP (V)[a]			
	RP(exp)	OP(exp)	EA(M⁻)	IP(M⁺)	IP(M⁺⁺)	IP(M²⁺)	RP(M⁻)	OP(M⁺)	OP(M²⁺)	OP(M⁺⁺)
1a	-1.594	0.686	-0.112	0.202	0.210	0.412	-1.606	0.606	0.580	0.504
1b	-1.781	0.367	-0.105	0.180	0.190	0.370	-1.788	0.283	0.264	0.251
1c	-1.771	0.219	-0.105	0.179	0.188	0.366	-1.788	0.268	0.234	0.226
1d	-1.779	0.226	-0.107	0.182	0.201	0.383	-1.736	0.312	0.361	0.390
2a	-2.071	0.592	-0.094	0.199	0.193	0.392	-2.073	0.562	0.429	0.289
2b	-2.170	0.261	-0.088	0.176	0.182	0.358	-2.229	0.224	0.173	0.150
2c	-	0.144	-0.086	0.171	0.185	0.356	-2.281	0.150	0.158	0.188
2d	-	0.154	-0.088	0.178	0.181	0.359	-2.229	0.253	0.181	0.137
3a	-1.458	0.660	-0.118	0.203	0.234	0.437	-1.450	0.620	0.768	0.808
3b	-1.620	0.353	-0.112	0.179	0.194	0.373	-1.606	0.268	0.286	0.302
3c	-1.609	0.215	-0.111	0.177	0.186	0.362	-1.632	0.239	0.203	0.200
3d	-1.611	0.222	-0.113	0.182	0.191	0.373	-1.580	0.312	0.286	0.264
4a	-1.696	0.630	-0.107	0.201	0.215	0.416	-1.736	0.591	0.610	0.568
4b	-1.882	0.322	-0.101	0.182	0.199	0.381	-1.892	0.312	0.346	0.365
4c	-1.870	0.183	-0.101	0.180	0.197	0.377	-1.892	0.283	0.316	0.340

4d	-1.869	0.185	-0.103	0.184	0.197	0.380	-1.840	0.341	0.339	0.340
4e	-2.133	0.537	-0.093	0.199	0.206	0.404	-2.099	0.562	0.519	0.454
4f	-2.255	0.572	-0.087	0.197	0.197	0.395	-2.255	0.532	0.452	0.340
4g	-2.232	0.212	-0.089	0.180	0.202	0.381	-2.203	0.283	0.346	0.403
4h	-2.36	0.404	-0.084	0.175	0.182	0.357	-2.333	0.209	0.166	0.150
5a	-2.219	-0.063	-0.087	0.159	0.179	0.338	-2.255	-0.026	0.023	0.112
5b	-2.421	-0.115	-0.080	0.150	0.177	0.327	-2.437	-0.158	-0.060	0.086
5c	-2.598	-0.142	-0.075	0.147	0.167	0.314	-2.567	-0.202	-0.158	-0.040
MAD							**0.023**	**0.065**	**0.076**	**0.124**

a Equations 3 - 6 used, obtained from the relationships in Figure 14.

3.2.4 Prediction of the reduction and oxidation potential from MESP potentials

The relationship between the different MESP properties with their experimental RP and OP were carried out and the results of the best correlations obtained are shown in Figure 15 (a – d), with data in Table 4. The analysis clearly showed that experimental RP correlates well with potentials of the reduced state, with $V_{min}(M^-)$ ($R^2 = 0.71$) and also $V(Mo,M^-)$ ($R^2 = 0.68$) (Figure 15c and d). The experimental OP was best correlated with the potentials of the neutral state, potential $V(Mo,M)$ ($R^2 = 0.78$) and $V(C,M)$ ($R^2 = 0.70$) (Figure 15a and b), in contrast to their oxidized states M^+ ($R^2 = 0.62$ and 0.57) and M^{2+} ($R^2 = 0.45$ and 0.32) (not shown). The experimental oxidation potential has a poor correlation with V_{min} of the neutral state. In all the states, the V_{max} has a poor correlation with both experimental RP and OP.

The best fit obtained linear regression equations for the correlation of the experiment RP and experimental OP with MESP potentials, are

OP(exp) = 5.775 x(V(Mo,M)) + 269.84 $\quad$ ($R^2 = 0.78$) $\qquad$ Equation 7

OP(exp) = 5.786 x (V(C,M)) + 84.96 $\qquad$ ($R^2 = 0.70$) $\qquad$ Equation 8

RP(exp) = 0.035 x ($V_{min}(M^-)$) + 1.619 $\quad$ ($R^2 = 0.71$) $\qquad$ Equation 9

RP(exp) = 11.897 x (V(Mo,M$^-$)) + 555.46 $\quad$ ($R^2 = 0.68$) $\qquad$ Equation 10

The above equations can be used to predict the experimental OP and RP, similarly as calculated IP and EA values were used to predict experimental OP and RP in section 3.2.3, see predicted data in Table 4. The advantage of using equations 7 and 8 is that OP can be predicted from a calculation on the neutral molecule only and that it is not necessary to calculate an oxidized state to obtain IP as well. Calculating the predicted OP and RP using equations 7 - 10 above, reproduce the experimental values with a MAD of 0.085, 0.108, 0.143 and 0.146 respectively. Using equation 7 or 8 (MAD = 0.085, 0.108) thus reproduces the experimental OP better than the calculated OP (Table 1, B3LYP) for M^+ (MAD = 0.394), M^{++} (MAD = 0.214) and M^{2+} (MAD = 0.196). Using equations 9 and 10, reproduces the experimental RP with a MAD of 0.143 and 0.146, while predicting the RP from equation 3 (Table 3, MAD = 0.023) or the calculated RP (Table 1, B3LYP) with a MAD = 0.124, which gives a better result.
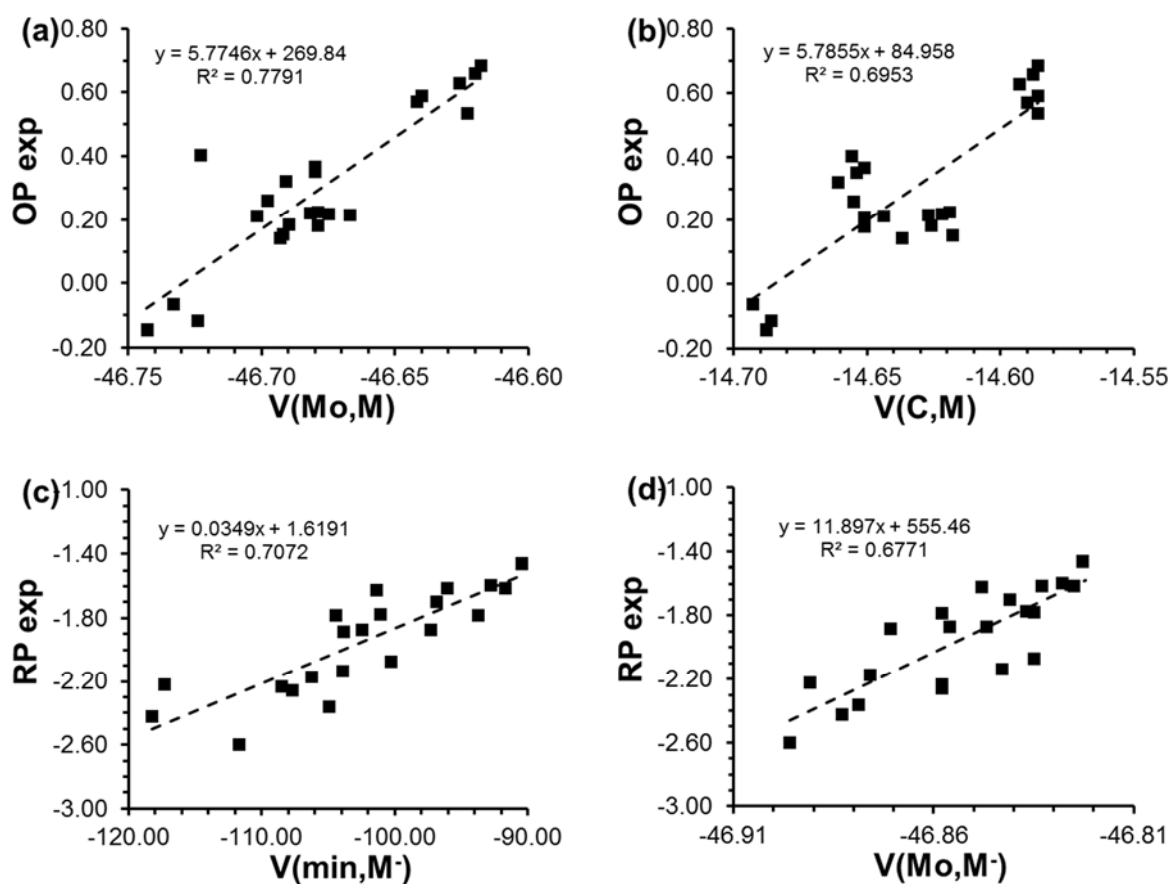
Figure 15: The selected best representative correlation plots of the experimental oxidation potential (OP in V) and reduction potential (RP in V) with MESP properties (a) V(Mo,M), (b) V(C,M), (c) $V_{min}(M^-)$ and (d) V(Mo,M$^-$) for the derivatives in the neutral (M), reduced (M$^-$) and oxidised (M$^+$, M^{2+}) states. The V_{min} is reported in kcal/mol, atomic potential Mo (V(Mo)) and carbene carbon (V(C)) are in the atomic unit.

Table 4: Selected MESP potentials, experimental 1e⁻ RP and 2e⁻ OP with the predicted 1e⁻ RP and 2e⁻ OP (in V) from the indicated calculated MESP potentials using B3LYP in acetonitrile solution. V_{min} is reported in kcal/mol, the atomic potential Mo (V(Mo)) and carbene carbon (V(C)) are in the atomic unit.

Mol	Experimental RP and OP (V)		Calculated MESP potential V_{min} (kcal/mol) and V(atom) (au).				Predicted RP and OP (V)[a]			
	OP(exp)	RP(exp)	V(Mo,M)	V(C,M)	V_{min}(M⁻)	V(Mo,M⁻)	OP (V(Mo,M))	OP (V(C,M))	RP (V_{min}(M⁻))	RP (V(Mo,M⁻))
1a	0.686	-1.594	-46.618	-14.586	-92.84	-46.828	0.640	0.571	-1.621	-1.653
1b	0.367	-1.781	-46.680	-14.651	-104.47	-46.858	0.282	0.195	-2.027	-2.010
1c	0.219	-1.771	-46.675	-14.627	-101.08	-46.837	0.311	0.333	-1.909	-1.760
1d	0.226	-1.779	-46.679	-14.619	-93.73	-46.835	0.287	0.380	-1.652	-1.736
2a	0.592	-2.071	-46.640	-14.586	-100.33	-46.835	0.513	0.571	-1.882	-1.736
2b	0.261	-2.170	-46.698	-14.655	-106.27	-46.876	0.178	0.171	-2.090	-2.224
2c	0.144		-46.693	-14.637	-104.54	-46.862	0.207	0.276	-2.029	-2.057
2d	0.154		-46.692	-14.618	-112.67	-46.822	0.212	0.386	-2.313	-1.581
3a	0.660	-1.458	-46.620	-14.588	-90.51	-46.823	0.628	0.559	-1.540	-1.593
3b	0.353	-1.620	-46.680	-14.654	-101.41	-46.848	0.282	0.177	-1.920	-1.891
3c	0.215	-1.609	-46.667	-14.644	-96.05	-46.825	0.357	0.235	-1.733	-1.617
3d	0.222	-1.611	-46.682	-14.622	-91.69	-46.833	0.270	0.362	-1.581	-1.712
4a	0.630	-1.696	-46.626	-14.593	-96.92	-46.841	0.594	0.530	-1.763	-1.807
4b	0.322	-1.882	-46.691	-14.661	-103.90	-46.871	0.218	0.137	-2.007	-2.164
4c	0.183	-1.870	-46.679	-14.651	-102.48	-46.856	0.287	0.195	-1.957	-1.986

4d	0.185	-1.869	-46.690	-14.626	-97.30	-46.847	0.224	0.339	-1.777	-1.879
4e	0.537	-2.133	-46.623	-14.586	-103.96	-46.843	0.611	0.571	-2.009	-1.831
4f	0.572	-2.255	-46.642	-14.590	-107.72	-46.858	0.501	0.548	-2.140	-2.010
4g	0.212	-2.232	-46.702	-14.651	-108.52	-46.858	0.155	0.195	-2.168	-2.010
4h	0.404	-2.360	-46.723	-14.656	-104.95	-46.879	0.033	0.166	-2.044	-2.259
5a	-0.063	-2.219	-46.733	-14.693	-117.33	-46.891	-0.024	-0.048	-2.476	-2.402
5b	-0.115	-2.421	-46.724	-14.686	-118.24	-46.883	0.028	-0.008	-2.507	-2.307
5c	-0.142	-2.598	-46.743	-14.688	-111.70	-46.896	-0.082	-0.019	-2.279	-2.462
MAD							**0.085**	**0.108**	**0.143**	**0.146**

[a] Equations 7 - 10 used, obtained from the relationships in Figure 15.

3.3 Clustering of the complexes based on the similarity in properties

The multivariance analysis of the computed properties with the experimental RP and OP was carried out to show the level of their relationship and the grouping of the Mo carbene derivatives based on the similarity of their properties. The multivariance analysis was done using FactoMineR (Factor analysis and data Mining with R) [55]. The Mo carbene derivatives were grouped in clusters of those that have similar properties based on their experimental and computational RP and OP with their computed EA, IP, V_{min}, V(Mo), V(C), HOMO and the LUMO. The analysis was divided into five groups, showing the relationship between the properties of the molecules in their neutral state, reduced state, 1e$^-$ oxidation state and 2e$^-$ oxidation state (Figure 16). The fifth group relates the computed OP values determined for M^{++} states with the properties computed for the molecules in their M$^+$ electronic state (Figure S8). The clustering obtained for the first four groups is shown in Figure 16. The results of the variable distribution (experimental and computed properties) along the principal component analysis (PCA) show that EA has a reverse correlation with the RP (pointing in opposite direction) while the IP has a direct correlation with OP (pointing in the same direction) (Figure 16c and d). The computed HOMO, V(Mo) and V(C) of the molecules in their neutral state show better correlation with the experimental OP while the computed LUMO showed a better correlation with the experimental RP (Figure 16a). The calculated EA, RP and HOMO of the derivatives in M$^-$ state show the best correlation with experimental RP (Figure 16b). The experimental OP shows the best correlation with calculated IP, OP and LUMO in the M$^+$ state (Figure 16c) compared to that of M^{++} and M^{2+} states (using the alignment of their arrow with the colour of their contribution).

The clustering of the derivatives according to the similarities in their experimental and computed properties is shown in Figure 17 for their neutral, M$^-$, M$^+$ and M^{2+} states (see also Figure S8 for M^{++} state). The type of the carbene ligand did not have stronger effects on the correlation of the computed properties as the clustering of the complexes are not correlated according to the types of the carbene ligands. Rather, other ligands like dppe and the presence of unsubstituted CO play a stronger effect on the complex clustering than the carbene ligand type. Four clusterings of the derivatives are observed in all of the five states groupings; one cluster is formed mainly for the derivatives containing the dppe ligand (**5a-c**). The second cluster that is particular to all three oxidation states (M$^+$, M^{2+} and M^{++}), covers the derivatives with unsubstituted CO ligands (1a, 2a, 4a, 4e, 4f), excluding **3a**. In the group M$^+$ that showed the better correlation with experimental OP than M^{2+} and M^{++}, the molecules with an SbPh$_3$ ligand (**1d**, **2d**, **3d**, **4d**) formed a well-defined cluster separated from the rest of the other molecules. The clustering of the molecules in their reduced state is different from those of the

31

oxidized state except the common cluster of complexes with dppe ligand. The second cluster in a reduced state is best described in terms of molecules with NH_2 and NHCy carbene substituents (**4e, 4f, 4g, 4h**) compared to an oxidized state that is more influenced by the presence of unsubstituted CO.
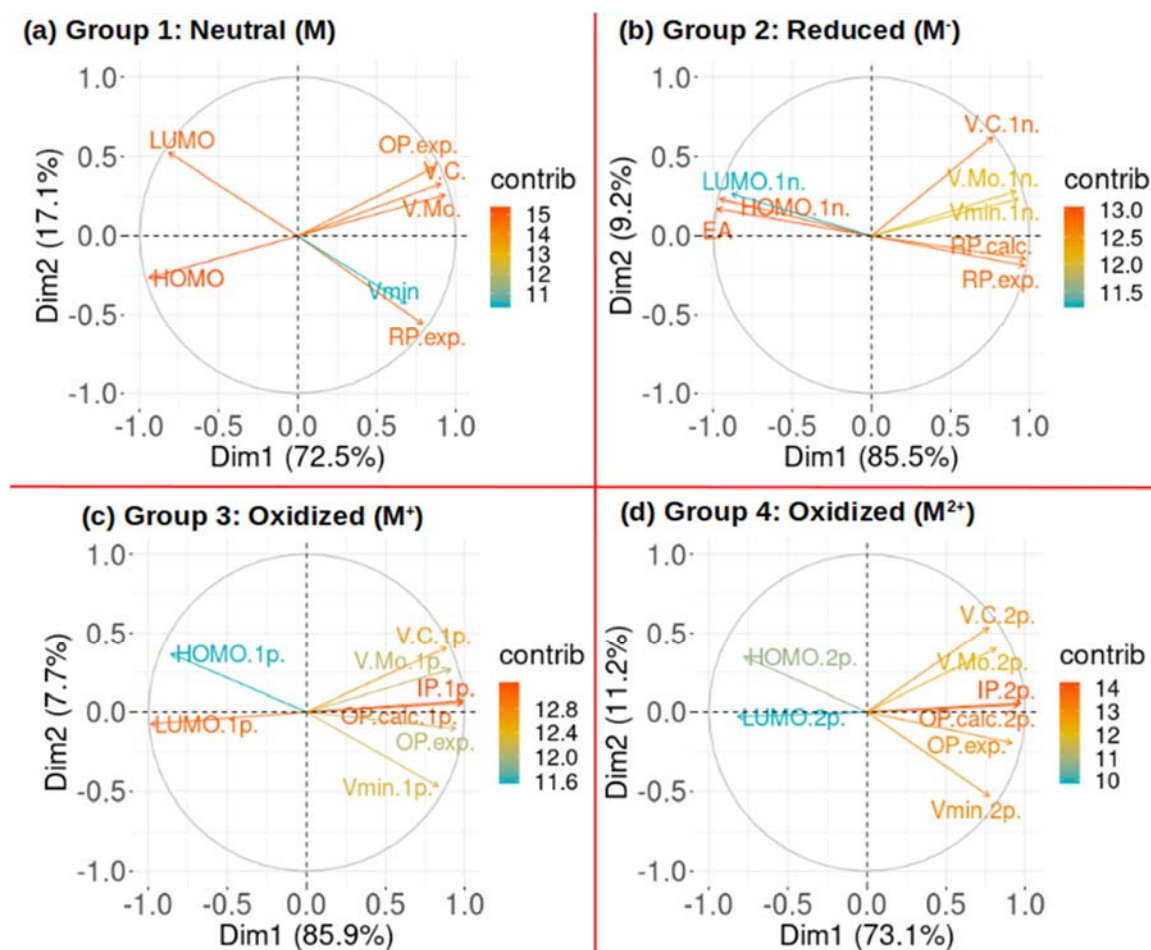

Figure 16: The distribution of the variables MESP minimum (V_{min}), Mo atomic potential ($V(Mo)$), carbene C atomic potential ($V(C)$), HOMO and LUMO energies, calculated for the (a) neutral molecules (1n) and related to experimental RP and OP, (b) reduced molecules and related to experimental RP and calculated electron affinity (EA) and RP also at M^- state; (c) M^+ oxidized molecules (1p) and related to the experimental OP and calculated OP and ionization potential (IP) also at M^+ state, (d) M^{2+} oxidized molecules (2p) and related to the experimental OP and the calculated OP and IP also at M^{2+} state
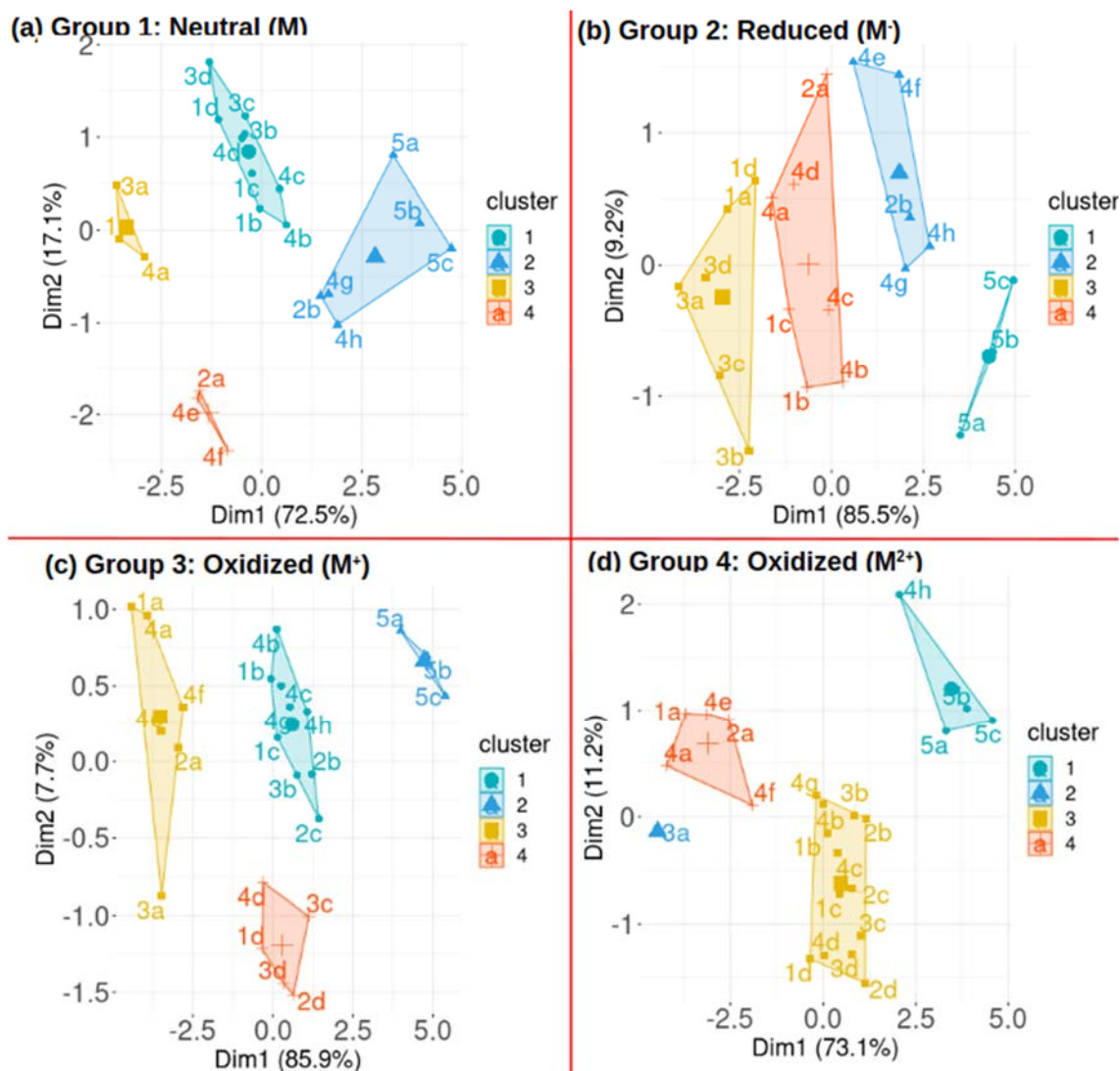
Figure 17: The partitioning clustering of the Mo carbene derivatives based on the values of the variables MESP minimum (V_{min}), Mo atomic potential ($V(Mo)$), carbene C atomic potential ($V(C)$), HOMO and LUMO energies, calculated for the (a) neutral molecules (1n) and related to experimental RP and OP, (b) reduced molecules and related to experimental RP and calculated electron affinity (EA) and RP also at M^- state; (c) M^+ oxidized molecules (1p) and related to the experimental OP and calculated OP and ionization potential (IP) also at M^+ state, (d) M^{2+} oxidized molecules (2p) and related to the experimental OP and the calculated OP and IP also at M^{2+} state.

4   Conclusion

A DFT study of 23 derivatives of Mo Fischer carbene complexes of the type $[Mo(CO)_n(L_{n-5})\{C(Y)Ar\}]$ (n = 3-5, Ar = aryl group) and Y = OEt, NH_2 or NHCy, grouped into 5 models which

comprise derivatives of 2-thienyl (model 1), 2-(N-methyl)pyrrolyl) (model 2), 2-(2-thienyl)thiophene (model 3), 2-furyl derivatives (model 4) and 2-furyl with a diphenyl phosphinoethane (dppe) ligand (model 5), showed that several DFT calculated descriptors can be used to predict the 1e⁻ reduction and 2e⁻ oxidation potentials (RP and OP) of the Mo Fischer carbene complexes.

- Calculating the RP and OP using the energy cycle of solvation shown in Figure 2, reproduced the RP and OP to MAD values of 0.124-0.151 and 0.196-0.421 respectively, depending on the level of theory (B3LYP or M06) and type of model (M^- for reduction and M^+, M^{++} or M^{2+} for oxidation).

- Calculating the RP and OP using the LUMO (for RP) and HOMO (for OP) energies of the neutral carbenes, using equations 1 and 2, the RP and OP of the carbenes can be predicted to a MAD value of 0.058 (RP) and 0.104 (OP) respectively.

- Calculating the RP and OP using the calculated EA and IP (of M^+, M^{2+} and M^{++}) energies, using equations 3 - 6, reproduced the experimental values with a MAD value of 0.023 (RP), 0.065, 0.076 and 0.124 (OP) respectively.

- Calculating the predicted OP and RP using MESP potentials using equations 7 - 10, reproduced the experimental values with a MAD of 0.143 and 0.146 for RP and 0.085 and 0.108 for OP.

- The most accurate prediction of RP and OP of the Mo Fischer carbene complexes, according to the MAD values, is obtained from B3LYP in acetonitrile calculated EA (for RP with MAD 0.023) and IP (for OP with MAD 0.065) calculated energies, followed by the prediction of RP and OP from the LUMO (for RP with MAD 0.058) and HOMO (for OP with MAD 0.104) energies of the neutral carbenes.

- Calculation of the LUMO and HOMO energies of the neutral carbenes involved optimizing only the neutral carbene, while the calculation of the RP and OP, or calculation of IP and EA values, also needed optimization of the reduced and oxidized carbenes, more than double the amount of calculations additionally. Because of the cost of CPU hours, predicting RP and OP from the LUMO and HOMO energy of the neutral carbenes respectively, is a much faster, easier and cheaper, but slightly less accurate method but good enough to give the predictive trend of change in the redox properties of the complexes.

CRediT author Statement

A.A. Adeniyi: Conceptualization, Methodology, Validation, Formal analysis, Investigation, Data curation, Writing – original draft preparation & editing, Visualization.

M. Landman: Writing – review & editing.

J. Conradie: Conceptualization, Methodology, Resources, Validation, Writing – review & editing, Supervision, Funding acquisition, Project administration.

σ

Ethical Statement/Conflict of Interest

This work does not require any ethical statement and there is no conflict of interest.

References

[1]   E.O. Fischer, A. Maasböl, On the Existence of a Tungsten Carbonyl Carbene Complex, Angew. Chemie Int. Ed. English. 3 (1964) 580–581. doi:10.1002/anie.196405801.

[2]   T.R. Hoye, G.M. Rehberg, Manganese Fischer Carbene Chemistry: Reactions of Cp'(CO)$_2$Mn=C(OMe/OLi)R with Enynes, 1-Hexyne, and Acrylates, Organometallics. 9 (1990) 3014–3015. doi:10.1021/om00162a005.

[3]   D. Vuzman, E. Poverenov, Y. Diskin-Posner, G. Leitus, L.J.W. Shimon, D. Milstein, Reactivity and stability of platinum(II) formyl complexes based on PCP-type ligands. The significance of sterics, Dalt. Trans. (2007) 5692. doi:10.1039/b711444c.

[4]   D. Kremzow, G. Seidel, C.W. Lehmann, A. Fürstner, Diaminocarbene- and Fischer-Carbene Complexes of Palladium and Nickel by Oxidative Insertion: Preparation, Structure, and Catalytic Activity, Chem. - A Eur. J. 11 (2005) 1833–1853. doi:10.1002/chem.200400928.

[5]   K.H. Dötz, J. Stendel, Fischer Carbene Complexes in Organic Synthesis: Metal-Assisted and Metal-Templated Reactions, Chem. Rev. 109 (2009) 3227–3274. doi:10.1021/cr900034e.

[6]   W.D. Wulff, B.M. Bax, T.A. Brandvold, K.S. Chan, A.M. Gilbert, R.P. Hsung, J. Mitchell, J. Clardy, Reactions of Group 6 Fischer carbene complexes with alkynes: effect of the metal on the product distribution and the isolation of a nontautomerized cyclohexadienone complex, Organometallics. 13 (1994) 102–126. doi:10.1021/om00013a021.

[7]   J. Barluenga, J. Santamaría, M. Tomás, Synthesis of Heterocycles via Group VI Fischer Carbene Complexes, Chem. Rev. 104 (2004) 2259–2284. doi:10.1021/cr0306079.

[8]   D. F. Harvey, M. F. Brown, Molybdenum carbene complexes: Cyclopropanation of electron-poor olefins, Tetrahedron Lett. 31 (1990) 2529–2532. doi:10.1016/0040-4039(90)80117-5.

[9]   E.O. Fischer, A. Maasböl, Übergangsmetall-Carben-Komplexe, II. Phenylmethoxycarben- und Methylmethoxycarben-pentacarbonyl-chrom, -molybdän, -wolfram und -

cyclopentadienyl-dicarbonyl-mangan, Chem. Ber. 100 (1967) 2445–2456. doi:10.1002/cber.19671000744.

[10] E.O. Fischer, R. Aumann, Übergangsmetall-Carben-Komplexe, XI. Über die Darstellung voncis-M(C6H5)3-Methoxy-organylcarben-metall-tetracarbonyl-Komplexen (M = P, As, Sb) des Chroms, Molybdäns und Wolframs aus den M(C$_6$H$_5$)$_3$-Metall-pentacarbonylen durch CH^{3-}/CH3$^+$-Addition, Chem. Ber. 102 (1969) 1495–1503. doi:10.1002/cber.19691020509.

[11] K.H. Dötz, H. Larbig, K. Harms, Reaktionen von Komplexliganden, LI. Synthese und Reaktionen stabiler (Carben)tetracarbonyl-Chelatkomplexe des Molybdäns, Chem. Ber. 125 (1992) 2143–2148. doi:10.1002/cber.19921250924.

[12] J. Barluenga, K. Muñiz, M. Tomás, A. Ballesteros, S. García-Granda, A Simple Approach toward Enantiomerically Pure Fischer Carbene Complexes of Chromium and Molybdenum: Chiral Modification of the Metal Fragment, Organometallics. 22 (2003) 1756–1760. doi:10.1021/om0210560.

[13] J. Powell, D.H. Farrar, S.J. Smith, Synthesis and structural characterization of a stable hydroxycarbene, Inorganica Chim. Acta. 85 (1984) L23–L25. doi:10.1016/S0020-1693(00)81013-0.

[14] G. Erker, U. Dorf, C. Krueger, Y.H. Tsay, Uncommon structural features of [Cp$_2$ZrOCPhMo(CO)$_5$]$_2$O, a zirconium-oxygen-zirconium-bridged tetranuclear bis(carbene)metal complex exhibiting a planar .sigma.-framework, Organometallics. 6 (1987) 680–682. doi:10.1021/om00146a043.

[15] A. Jansen van Rensburg, M. Landman, P.H. van Rooyen, M.M. Conradie, J. Conradie, Molybdenum(0) Fischer ethoxycarbene complexes: Synthesis, X-ray crystal structures and DFT study, Polyhedron. 121 (2017) 285–296. doi:10.1016/j.poly.2016.10.013.

[16] A. Jansen van Rensburg, M. Landman, P.H. van Rooyen, M.M. Conradie, E. Erasmus, J. Conradie, Structural and electronic features of triphenylstibine-functionalized Fischer carbene complexes of molybdenum(0), Polyhedron. 133 (2017). doi:10.1016/j.poly.2017.05.042.

[17] M. Landman, H. Görls, S. Lotz, Synthesis of Molybdenum Carbene Complexes of Thiophene Derivatives, Zeitschrift Für Anorg. Und Allg. Chemie. 628 (2002) 2037–2043. doi:10.1002/1521-3749(200209)628:9/10<2037::AID-ZAAC2037>3.0.CO;2-T.

[18] M. Landman, T. Levell, P.H. van Rooyen, J. Conradie, Conformation analysis of triphenylphosphine in trans and cis triphenylphosphine-substituted Fischer carbene complexes, J. Mol. Struct. 1065–1066 (2014) 29–38. doi:10.1016/j.molstruc.2014.02.014.

[19] M. Landman, T.J. Levell, M.M. Conradie, P.H. Van Rooyen, J. Conradie, Structural and conformational study of pentacarbonyl and phosphine substituted Fischer alkoxy- and aminocarbene complexes of molybdenum, J. Mol. Struct. 1086 (2015) 190–200. doi:10.1016/j.molstruc.2015.01.022.

[20] M. Landman, J. Conradie, E versus Z isomers of Fischer aminocarbene complex [Mo(CO)$_4$(PPh$_3$){C(NHCy)(2-furyl)}]: NH···O versus CH···O intramolecular hydrogen bonds, J. Mol. Struct. 1094 (2015) 36–45. doi:10.1016/j.molstruc.2015.04.001.

[21] R. Schobert, R. Kempe, T. Schmalz, A. Gmeiner, Syntheses, structures and electrochemistry of some 1-(η^2-allylamino)-1-ferrocenylcarbene complexes of chromium(0), molybdenum(0) and tungsten(0), J. Organomet. Chem. 691 (2006) 859–868. doi:10.1016/j.jorganchem.2005.10.047.

[22] C. Sandoval-Chávez, J.G. López-Cortés, A.I. Gutiérrez-Hernández, M.C. Ortega-Alfaro, A. Toscano, C. Alvarez-Toledano, An expedient approach to ferrocenyl thioamides via Fischer carbenes, J. Organomet. Chem. 694 (2009) 3692–3700. doi:10.1016/j.jorganchem.2009.07.044.

[23] I. Hoskovcová, J. Ludvík, Electrochemical approach to Fischer carbene complexes, Curr. Opin. Electrochem. 15 (2019) 165–174. doi:10.1016/j.coelec.2019.06.005.

[24] A. Jansen van Rensburg, M. Landman, M.M. Conradie, E. Erasmus, J. Conradie, Electrochemistry of triphenylstibine-functionalized Fischer carbene complexes of

Molybdenum(0), Electrochim. Acta. 246 (2017) 897–907. doi:10.1016/j.electacta.2017.06.103.

[25] M. Landman, T.J. Levell, B.E. Buitendach, M.M. Conradie, J. Conradie, Effect of CO substitution on the redox properties of Fischer Mo(0) carbene complexes $Mo(CO)_5=C(Y)(2-Furyl)$, Y = OEt, NHCy or NH_2, Electrochim. Acta. 174 (2015) 282–289. doi:10.1016/j.electacta.2015.05.191.

[26] M.J. Frisch, G.W. Trucks, H.B. Schlegel, G.E. Scuseria, M.A. Robb, J.R. Cheeseman, G. Scalmani, V. Barone, G.A. Petersson, X. Nakatsuji, H.; Li, M. Caricato, A. V. Marenich, J. Bloino, B.G. Janesko, R. Gomperts, B. Mennucci, H.P. Hratchian, J. V. Ortiz, A.F. Izmaylov, J.L. Sonnenberg, D. Williams-Young, F. Ding, F. Lipparini, F. Egidi, J. Goings, B. Peng, A. Petrone, T. Henderson, D. Ranasinghe, V.G. Zakrzewski, J. Gao, N. Rega, G. Zheng, W. Liang, M. Hada, M. Ehara, K. Toyota, R. Fukuda, J. Hasegawa, M. Ishida, T. Nakajima, Y. Honda, O. Kitao, H. Nakai, T. Vreven, K. Throssell, J. Montgomery, J. A., J.E. Peralta, F. Ogliaro, M.J. Bearpark, J.J. Heyd, E.N. Brothers, K.N. Kudin, V.N. Staroverov, T.A. Keith, R. Kobayashi, J. Normand, K. Raghavachari, A.P. Rendell, J.C. Burant, S.S. Iyengar, J. Tomasi, M. Cossi, J.M. Millam, M. Klene, C. Adamo, R. Cammi, J.W. Ochterski, R.L. Martin, K. Morokuma, O. Farkas, J.B. Foresman, D.J. Fox, Gaussian 16, Revision C.01, (2016).

[27] F. Weigend, R. Ahlrichs, Balanced basis sets of split valence, triple zeta valence and quadruple zeta valence quality for H to Rn: Design and assessment of accuracy, Phys. Chem. Chem. Phys. 7 (2005) 3297. doi:10.1039/b508541a.

[28] Chemcraft - graphical software for visualization of quantum chemistry computations., (n.d.). http://www.chemcraftprog.com/.

[29] A.A. Adeniyi, J. Conradie, Electronic effect of β-diketonato ligands on the redox potential of fac and mer tris(β-diketonato) iron(III) complexes: A density functional theory study and molecular electrostatic potential analysis, Int. J. Quantum Chem. e26036 (2019) 1–14.

[30] A.A. Adeniyi, J. Conradie, Influence of substituents on the reduction potential and pKa values of β-diketones tautomers: A theoretical study, Electrochim. Acta. 297 (2019) 947–960. doi:10.1016/j.electacta.2018.12.030.

[31] A.A. Adeniyi, J. Conradie, Computational insight into the contribution of para-substituents on the reduction potential, proton affinity, and electronic properties of nitrobenzene compounds, J. Mol. Model. 25 (2019) 78. doi:10.1007/s00894-019-3946-2.

[32] A. V Marenich, J. Ho, M.L. Coote, C.J. Cramer, D.G. Truhlar, Computational electrochemistry : prediction of liquid-phase reduction potentials †, Phys. Chem. Chem. Phys. 16 (2014) 15068–15106. doi:10.1039/c4cp01572j.

[33] M. Namazian, C.Y. Lin, M.L. Coote, Benchmark Calculations of Absolute Reduction Potential of Ferricinium / Ferrocene Couple in Nonaqueous Solutions, J. Chem. Theory Comput. 6 (2010) 2721–2725. doi:10.1021/ct1003252.

[34] Y. Zhao, D.G. Truhlar, A new local density functional for main-group thermochemistry , transition metal bonding , thermochemical kinetics , and noncovalent interactions A new local density functional for main-group thermochemistry , transition metal bonding , thermochemical kin, J. Chem. Phys. 125 (2006) 194101. doi:10.1063/1.2370993.

[35] A. V Marenich, C.J. Cramer, D.G. Truhlar, Universal Solvation Model Based on Solute Electron Density and on a Continuum Model of the Solvent Defined by the Bulk Dielectric Constant and Atomic Surface Tensions, J. Phys. Chem. B. 113 (2009) 6378–6396.

[36] R.E. Skyner, J.L. Mcdonagh, C.R. Groom, T. Van Mourik, A review of methods for the calculation of solution free energies and the modelling of systems in solution, Phys. Chem. Chem. Phys. 17 (2015) 6174–6191. doi:10.1039/C5CP00288E.

[37] S.R. Gadre, R.K. Pathak, Nonexistence of local maxima in molecular electrostatic potential maps, Proc. Indian Acad. Sci. - Chem. Sci. 102 (1990) 189–192. doi:10.1007/BF02860157.

[38] S.R. Gadre, S.A. Kulkarni, R.K. Pathak, Reply to the comment on: Maximal and minimal characteristics of molecular electrostatic potentials: Some further extensions [2], J. Chem.

Phys. 94 (1991) 8639. doi:10.1063/1.460055.

[39] S.R. Gadre, S.A. Kulkarni, I.H. Shrivastava, Molecular electrostatic potentials: A topographical study, J. Chem. Phys. 96 (1992) 5253–5260. doi:10.1063/1.462710.

[40] P. Politzer, J.S. Murray, The fundamental nature and role of the electrostatic potential in atoms and molecules, Theor. Chem. Acc. 108 (2002) 134–142. doi:10.1007/s00214-002-0363-9.

[41] T. Lu, F. Chen, Multiwfn: a multifunctional wavefunction analyzer., J. Comput. Chem. 33 (2012) 580–592. doi:10.1002/jcc.22885.

[42] T. Lu, F. Chen, Quantitative analysis of molecular surface based on improved Marching Tetrahedra algorithm, J. Mol. Graph. Model. 38 (2012) 314–323. doi:https://doi.org/10.1016/j.jmgm.2012.07.004.

[43] S.R. Gadre, R.N. Shirsat, Electrostatics of Atoms and Molecules, Universities Press, India, 2001.

[44] P. Politzer, J.S. Murray, Z. Peralta-Inga, Molecular surface electrostatic potentials in relation to noncovalent interactions in biological systems, Int. J. Quantum Chem. 85 (2001) 676–684. doi:10.1002/qua.1706.

[45] W. Li, N. Yang, Y. Lyu, A mechanistic study on guanidine-catalyzed chemical fixation of CO_2 with 2-aminobenzonitrile to quinazoline-2,4(1: H,3 H)-dione, Org. Chem. Front. 3 (2016) 823–835. doi:10.1039/c6qo00085a.

[46] D. Kaur, R. Kaur, Theoretical Characterization of Hydrogen Bonding Interactions between RCHO (R = H, CN, CF_3, OCH_3, NH_2) and HOR′(R′ = H, Cl, CH_3, NH_2, C(O)H, C_6H_5), J. Chem. Sci. 127 (2015) 1299–1313. doi:10.1007/s12039-015-0885-z.

[47] W. Humphrey, A. Dalke, K. Schulten, VMD: visual molecular dynamics., J. Mol. Graph. 14 (1996) 27-28,33-38.

[48] M.K. Lloyd, J.A. McCleverty, D.G. Orchard, J.A. Connor, M.B. Hall, I.H. Hillier, E.M. Jones, G.K. McEwen, Electrochemical oxidation of organometallic complexes. Carbene and Lewis base complexes of chromium, molybdenum, and tungsten carbonyls, J. Chem. Soc. Dalt. Trans. (1973) 1743–1747. doi:10.1039/DT9730001743.

[49] A.J. van Rensburg, M. Landman, E. Erasmus, D. van der Westhuizen, H. Ferreira, M.M. Conradie, J. Conradie, Electrochemical and X-ray photoelectron spectroscopic insights into Molybdenum(0) Fischer ethoxycarbene complexes, Electrochim. Acta. 219 (2016) 204–213. doi:10.1016/j.electacta.2016.09.143.

[50] M. Landman, T.J. Levell, M.M. Conradie, P.H. van Rooyen, J. Conradie, Structural and conformational study of pentacarbonyl and phosphine substituted Fischer alkoxy- and aminocarbene complexes of molybdenum, J. Mol. Struct. 1086 (2015) 190–200. doi:10.1016/j.molstruc.2015.01.022.

[51] R. Gostynski, R. Fraser, M. Landman, E. Erasmus, J. Conradie, Electrochemical study of chromium(0) Fischer carbene complexes: Trends in redox potential, Polyhedron. 127 (2017) 323–330. doi:10.1016/j.poly.2017.02.018.

[52] B.A. Anjali, C.H. Suresh, Electronic effect of ligands vs. reduction potentials of Fischer carbene complexes of chromium: a molecular electrostatic potential analysis, New J. Chem. 42 (2018) 18217–18224. doi:10.1039/C8NJ04184A.

[53] G.S. Remya, C.H. Suresh, Assessment of the electron donor properties of substituted phenanthroline ligands in molybdenum carbonyl complexes using molecular electrostatic potentials, New J. Chem. 42 (2018) 3602–3608. doi:10.1039/C7NJ04592A.

[54] B.A. Anjali, F.B. Sayyed, C.H. Suresh, Correlation and Prediction of Redox Potentials of Hydrogen Evolution Mononuclear Cobalt Catalysts via Molecular Electrostatic Potential: A DFT Study, J. Phys. Chem. A. 120 (2016) 1112–1119. doi:10.1021/acs.jpca.5b11543.

[55] S. Lê, J. Josse, F. Husson, FactoMineR : An R Package for Multivariate Analysis, J. Stat. Softw. 25 (2008) 1–18. doi:10.18637/jss.v025.i01.